On entanglement Hamiltonians of an interval in massless harmonic chains

Giuseppe Di Giulio and Erik Tonni

SISSA and INFN Sezione di Trieste, via Bonomea 265, 34136 Trieste, Italy
E-mail: gdigiuli@sissa.it and etonni@sissa.it

Abstract. We study the continuum limit of the entanglement Hamiltonians of a block of consecutive sites in massless harmonic chains. This block is either in the chain on the infinite line or at the beginning of a chain on the semi-infinite line with Dirichlet boundary conditions imposed at its origin. The entanglement Hamiltonians of the interval predicted by conformal field theory (CFT) for the massless scalar field are obtained in the continuum limit. We also study the corresponding entanglement spectra, and the numerical results for the ratios of the gaps are compatible with the operator content of the boundary CFT of a massless scalar field with Neumann boundary conditions imposed along the boundaries introduced around the entangling points by the regularisation procedure.

Keywords: entanglement in extended quantum systems, solvable lattice models, conformal field theory

Contents

1. Introduction

Entanglement has attracted intense research activity during the last two decades, mostly focused on theoretical approaches [1–4], but in the last few years experimental setups have also been realised to detect its characteristic features [5].

Given a quantum system in a state described by the density matrix ρ, assuming that its Hilbert space can be factorised as $\mathcal{H} = \mathcal{H}_A \otimes \mathcal{H}_B$, the reduced density matrix ρ_A is defined by tracing out the degrees of freedom of $\mathcal{H}_B$, namely by $\rho_A = \mathrm{Tr}_{\mathcal{H}_B}\rho$, with the normalisation condition $\mathrm{Tr}_{\mathcal{H}_A}\rho_A = 1$. The reduced density matrix can be written as $\rho_A = \mathrm{e}^{-K_A}/\mathcal{Z}_A$, where the Hermitian operator K_A is the entanglement Hamiltonian (also known as the modular Hamiltonian) and $\mathcal{Z}_A = \mathrm{Tr}_{\mathcal{H}_A}\mathrm{e}^{-K_A}$. The entanglement entropy is easily obtained from the eigenvalues of ρ_A [6–8]. Important results have been obtained for factorisations of the Hilbert space corresponding to bipartitions $A \cup B$ of the space, namely when A is a spatial region and B its complement. In these cases the hypersurface $\partial A = \partial B$ separating A and B is called the entangling hypersurface.

A fundamental theorem proved by Bisognano and Wichmann [9] in the context of algebraic quantum field theory (QFT) claims that, given a relativistic QFT in $d+1$ dimensions in its vacuum state (we denote by $\boldsymbol{x}$ the d-dimensional position vector) and the spatial bipartition where A corresponds to a half space and the entangling hypersurface is the flat hyperplane, the entanglement Hamiltonian of A can be written as an integral over the half space A of the energy density $T_{00}(\boldsymbol{x})$ of the QFT as follows

Figure 1. The spatial bipartitions considered in this manuscript: an interval A in the infinite line (left) and an interval A at the beginning of the semi-infinite line (right).

$$K_A = 2\pi \int_A x_1 \, T_{00}(\boldsymbol{x}) \, \mathrm{d}\boldsymbol{x}. \tag{1}$$

When the QFT is a conformal field theory (CFT), the conformal symmetry allows us to write analytic expressions for the entanglement Hamiltonians for simple spatial bipartitions, mainly at equilibrium [10–14] but also in a few cases out of equilibrium [13]. More complicated bipartitions require a detailed knowledge of the underlying CFT [15, 16].

In a $1 + 1$-dimensional CFT at equilibrium in its vacuum state, we consider bipartitions where A is an interval such that its entanglement Hamiltonian can be written as

$$K_A = \ell \int_A \beta(x) \, T_{00}(x) \, \mathrm{d}x \tag{2}$$

where ℓ is the length of A and $\beta(x)$ depends on the bipartition. In this manuscript we focus on the bipartitions shown in figure 1. For an interval in the infinite line (left panel in figure 1), the weight function in (2) is the following parabola [10, 11]

$$\beta(x) = 2\pi \, \frac{x}{\ell} \left(1 - \frac{x}{\ell} \right). \tag{3}$$

When A is an interval at the beginning of a semi-infinite line (right panel in figure 1), the weight function in (2) is the half parabola given by [13]

$$\beta(x) = \pi \left(\frac{x}{\ell} + 1 \right) \left(1 - \frac{x}{\ell} \right) \tag{4}$$

independently of the boundary conditions imposed at the beginning of the semi-infinite line. The continuum limit of a one-dimensional lattice model at its critical point is described by a 1+1 dimensional CFT. It is interesting to explore the procedure that leads to these entanglement Hamiltonians in a given CFT as the continuum limit of the corresponding entanglement Hamiltonians in the underlying lattice model.

Entanglement Hamiltonians in free lattice models at equilibrium in their ground state have been studied in [1, 2, 17–22]. A detailed analysis of the continuum limit has been recently carried out for an interval in an infinite chain of free fermions [22], by employing the analytical results obtained by Eisler and Peschel in [20]. In this manuscript we study the continuum limit of the entanglement Hamiltonians of a block of consecutive sites in massless harmonic chains by following the approach of [22], which is based on the observation that, in this limit, the proper combinations of all the diagonals of the matrices determining the entanglement Hamiltonian on the lattice must be considered [19].

The eigenvalues λ_j of the entanglement Hamiltonian provide the entanglement spectrum, which contains relevant physical information [23]. It is worth introducing the gaps $g_r \equiv \log \lambda_{\max} - \log \lambda_r$ with respect to the largest eigenvalue and also their

ratios g_r/g_1 with respect to the smallest gap g_1. We remark that these ratios are not influenced by a global shift and a rescaling of the entire spectrum.

In a two-dimensional QFT in imaginary time, a useful way to regularise the ultraviolet (UV) divergences consists of removing infinitesimal disks whose radius is the UV cutoff around the entangling points of the bipartition [7, 13, 18, 24]. In two-dimensional CFT, this regularisation procedure leads to a boundary conformal field theory (BCFT) [25] if proper conformal boundary conditions are imposed along the boundaries in the Euclidean spacetime (both the boundaries given by the physical boundaries of the system and the ones due to this regularisation procedure must be considered). For a class of entanglement Hamiltonians which includes the ones we are interested in, it has been found that [13]

$$\frac{g_r}{g_1} = \frac{\Delta_r}{\Delta_1} \tag{5}$$

where $r \geqslant 1$ and $\Delta_r > 0$ are the non-vanishing elements of the conformal spectrum (made by conformal dimensions of the primary fields and of their descendants) of the underlying BCFT. Numerical evidence that the conformal spectrum of a BCFT provides the entanglement spectrum were first obtained at equilibrium by Läuchli in [26] and more recently also out of equilibrium [27, 28].

In this manuscript we focus on massless harmonic chains and perform a numerical analysis of the continuum limit of two entanglement Hamiltonians of an interval A and of the corresponding entanglement spectra. We consider a massless harmonic chain both on the infinite line and on the semi-infinite line with Dirichlet boundary conditions imposed at its origin. The continuum limit of these lattice models is the CFT given by the massless scalar field Φ, whose central charge is $c = 1$. By introducing the canonical momentum field $\Pi = -\partial_t \Phi$, the energy density on the infinite line reads

$$T_{00}(x) = \frac{1}{2} \left[\Pi(x)^2 + \left(\partial_x \Phi(x) \right)^2 \right] \tag{6}$$

and on the semi-infinite line is given by [29]

$$T_{00}(x) = \frac{1}{2} \left[\Pi(x)^2 - \Phi(x) \, \partial_x^2 \Phi(x) \right]. \tag{7}$$

We study the spatial bipartitions shown in figure 1, whose entanglement Hamiltonians predicted by CFT are given by (2), (3) and (6) for the interval in the infinite line and by (2), (4) and (7) for the interval at the beginning of the semi-infinite line. Our numerical analysis is based on the procedure described in [20, 22] to study the continuum limit of the entanglement Hamiltonian of an interval in an infinite chain of free fermions. We also study the entanglement spectra of these entanglement Hamiltonians, finding that the CFT prediction (5) holds, once Neumann boundary conditions are imposed along the boundaries introduced by the regularisation procedure.

This manuscript is organised as follows. In section 2 we report the entanglement Hamiltonian of an interval in harmonic chains in terms of the two-point correlators. In section 3 we study the continuum limit of the entanglement Hamiltonian of an interval in the infinite line and in section 4 this analysis is performed for an interval at the beginning of the semi-infinite line with Dirichlet boundary conditions. In section 5 we

draw some conclusions. The appendix contains further results supporting some observations made in the main text.

2. Entanglement Hamiltonians in the harmonic chain

In this section we report the expression of the entanglement Hamiltonian of a subsystem in harmonic chains in terms of the two-point correlators [2], also discussing some decompositions that will be employed throughout the manuscript.

The Hamiltonian of the harmonic chain with nearest-neighbour spring-like interaction reads

$$\widehat{H} = \sum_i \left(\frac{1}{2m} \hat{p}_i^2 + \frac{m\omega^2}{2} \hat{q}_i^2 + \frac{\kappa}{2} (\hat{q}_{i+1} - \hat{q}_i)^2 \right)$$

(8)

where the position and the momentum operators $\hat{q}_i$ and $\hat{p}_i$ are Hermitean operators satisfying the canonical commutation relations $[\hat{q}_i, \hat{q}_j] = [\hat{p}_i, \hat{p}_j] = 0$ and $[\hat{q}_i, \hat{q}_j] = \mathrm{i}\delta_{i,j}$ ($\hbar = 1$ throughout this manuscript). In our numerical analysis we set $\kappa = m = 1$.

The Hamiltonian (8) is the discretisation of the Hamiltonian of a massive scalar field in the continuum, whose massless regime given by $\omega = 0$ is a CFT with central charge $c = 1$. The range of the index i in (8) depends on the spatial domain supporting the harmonic chain: in this manuscript we consider either the infinite line ($i \in \mathbb{Z}$) or the semi-infinite line (integer $i \geqslant 0$). When (8) is defined on the semi-infinite line, it is crucial to also specify the boundary condition imposed at the beginning of the semi-infinite line (i.e. at $i = 0$) and in our analysis we consider the case of Dirichlet boundary conditions. The two-point correlators $Q_{ij} = \langle \hat{q}_i \hat{q}_j \rangle$ and $P_{ij} = \langle \hat{p}_i \hat{p}_j \rangle$ provide the generic elements of the correlation matrices Q and P, respectively.

Let us consider harmonic chains (8) in their ground state $|0\rangle$ and introduce the bipartition of the chain into a spatial domain A made by L sites and its complement B, assuming that the Hilbert space can be bipartite accordingly as $\mathcal{H} = \mathcal{H}_A \otimes \mathcal{H}_B$. Since for these quantum systems the reduced density matrix $\rho_A \equiv \mathrm{Tr}_{\mathcal{H}_B}(|0\rangle\langle 0|)$ remains Gaussian, independently of the choice of the bipartition, the corresponding entanglement Hamiltonian $\widehat{K}_A$ is a quadratic Hermitian operator, which can be written as follows [2, 17]

$$\widehat{K}_A = \frac{1}{2} \hat{\boldsymbol{r}}^{\mathrm{t}} H_A \hat{\boldsymbol{r}} \qquad \hat{\boldsymbol{r}} = \begin{pmatrix} \hat{\boldsymbol{q}} \\ \hat{\boldsymbol{p}} \end{pmatrix}$$

(9)

where the $2L$-dimensional vector $\hat{\boldsymbol{r}}$ collects the position and the momentum operators $\hat{q}_i$ and $\hat{p}_i$ with $i \in A$. The matrix H_A is real, symmetric and positive-definite; hence $\widehat{K}_A$ is Hermitian. In terms of the reduced correlation matrices Q_A and P_A, obtained by restricting Q and P to the subsystem A, the matrix H_A can be evaluated as follows [2]

$$H_A = M \oplus N \equiv \left(h\big(\sqrt{P_A Q_A}\big) \oplus h\big(\sqrt{Q_A P_A}\big) \right) (P_A \oplus Q_A)$$
$$= (P_A \oplus Q_A) \left(h\big(\sqrt{Q_A P_A}\big) \oplus h\big(\sqrt{P_A Q_A}\big) \right)$$

(10)

where

$$h(y) \equiv \frac{1}{y} \log\left(\frac{y + 1/2}{y - 1/2}\right). \tag{11}$$

The equivalence of the two expressions in (10) can be verified by transposing one of them and employing that M and N are symmetric (we also need $(\sqrt{Q_A P_A})^{\mathrm{t}} = \sqrt{P_A Q_A}$, which is easily obtained from the fact that Q and P are symmetric).

In this manuscript we study entanglement Hamiltonians $\widehat{K}_A$ when the entire chain is at equilibrium in its ground state and when the subsystem A is a block of L consecutive sites either in the infinite line or at the beginning of the semi-infinite line where Dirichlet boundary conditions are imposed (see figure 1). In these two cases, the matrix H_A is block diagonal. The off-diagonal blocks of H_A can be non-vanishing e.g. for the time-dependent entanglement Hamiltonians after a global quantum quench [27].

The matrix H_A can be constructed numerically through (10) and (11). In order to employ these formulas, the eigenvalues of the matrix $\sqrt{Q_A P_A}$ must be strictly larger than $1/2$. In our numerical analysis many eigenvalues very close to $1/2$ occur and the software automatically approximates them to $1/2$ whenever a low numerical precision is set throughout the numerical analysis. This forces us to work with very high numerical precisions. In particular we have employed precisions up to 6500 digits, depending on the specific calculation. We observe that higher precision is required as L and ω increase. The fact that the numerical analysis of the entanglement Hamiltonian requires high numerical precisions has been already highlighted in [19, 20].

The expressions (9) and (10) naturally lead us to write the entanglement Hamiltonian in terms of the symmetric matrices M and N as follows

$$\widehat{K}_A = \frac{\widehat{H}_M + \widehat{H}_N}{2} \tag{12}$$

where

$$\widehat{H}_M \equiv \sum_{i,j=1}^{L} M_{i,j}\, \hat{q}_i\, \hat{q}_j \qquad \widehat{H}_N \equiv \sum_{i,j=1}^{L} N_{i,j}\, \hat{p}_i\, \hat{p}_j. \tag{13}$$

These sums can be organised in different ways. For instance, by writing the symmetric matrices M and N as sums of a diagonal matrix, an upper triangular matrix and a lower triangular matrix, it is straightforward to obtain

$$\widehat{H}_M = L \sum_{i=1}^{L} \left(\frac{M_{i,i}}{L} \hat{q}_i^2 + 2 \sum_{k=1}^{L-i} \frac{M_{i,i+k}}{L} \hat{q}_i\, \hat{q}_{i+k} \right) \tag{14}$$

$$\widehat{H}_N = L \sum_{i=1}^{L} \left(\frac{N_{i,i}}{L} \hat{p}_i^2 + 2 \sum_{k=1}^{L-i} \frac{N_{i,i+k}}{L} \hat{p}_i\, \hat{p}_{i+k} \right). \tag{15}$$

In [19] the sums (13) have been rewritten by decomposing the contribution coming from the ith row of the matrices M and N, and this leads to

$$\widehat{H}_M = L \sum_{i=1}^{L} \left(\frac{M_{i,i}}{L} \hat{q}_i^2 + \sum_{k=1}^{L-i} \frac{M_{i,i+k}}{L} \hat{q}_i \hat{q}_{i+k} + \sum_{k=1}^{i-1} \frac{M_{i,i-k}}{L} \hat{q}_i \hat{q}_{i-k} \right) \tag{16}$$

$$\widehat{H}_N = L \sum_{i=1}^{L} \left(\frac{N_{i,i}}{L} \hat{p}_i^2 + \sum_{k=1}^{L-i} \frac{N_{i,i+k}}{L} \hat{p}_i \hat{p}_{i+k} + \sum_{k=1}^{i-1} \frac{N_{i,i-k}}{L} \hat{p}_i \hat{p}_{i-k} \right). \tag{17}$$

We find it convenient to also introduce the following decomposition

$$\widehat{H}_M = L \left[\sum_{i=1}^{L/2} \left(\frac{M_{i,i}}{L} \hat{q}_i^2 + \sum_{k=1}^{L-2i+1} \frac{M_{i,i+k}}{L} \hat{q}_i \hat{q}_{i+k} \right) + \sum_{i=L/2+1}^{L} \left(\frac{M_{i,i}}{L} \hat{q}_i^2 + \sum_{k=1}^{2i-L-2} \frac{M_{i-k,i}}{L} \hat{q}_i \hat{q}_{i-k} \right) \right] \tag{18}$$

$$\widehat{H}_N = L \left[\sum_{i=1}^{L/2} \left(\frac{N_{i,i}}{L} \hat{p}_i^2 + \sum_{k=1}^{L-2i+1} \frac{N_{i,i+k}}{L} \hat{p}_i \hat{p}_{i+k} \right) + \sum_{i=L/2+1}^{L} \left(\frac{N_{i,i}}{L} \hat{p}_i^2 + \sum_{k=1}^{2i-L-2} \frac{N_{i-k,i}}{L} \hat{p}_i \hat{p}_{i-k} \right) \right] \tag{19}$$

where the contribution of the counter-diagonal has been included into the summation over $1 \leqslant i \leqslant L/2$. This choice leads to an inconsistency in the range of k of the last double sum when $i = L/2 + 1$, which can be easily fixed by imposing the vanishing of this term.

An alternative decomposition, inspired by the numerical analysis performed in [22], is discussed in the appendix. In our numerical analysis we have tested all the decompositions introduced above and in the appendix for both the spatial bipartitions shown in figure 1. In the main text we show the numerical results obtained from (18) and (19), while the results found through the other decompositions have been reported in the appendix.

The analytic results for the entanglement Hamiltonian of an interval in the infinite chain of free fermions found in [20, 22] and the decompositions introduced above for the operators $\widehat{H}_M$ and $\widehat{H}_N$ suggest introducing the following limits

$$\lim_{L\to\infty} \frac{M_{i,i+k}}{L} \equiv \mu_k(x_k) \qquad\qquad \lim_{L\to\infty} \frac{N_{i,i+k}}{L} \equiv \nu_k(x_k) \qquad\qquad x_k \equiv \frac{1}{L}\left(i + \frac{k}{2}\right) \tag{20}$$

where $i + k/2$ is the midpoint between the ith and the $(i + k)$th site. The existence of the functions μ_k and ν_k is a crucial assumption in the subsequent derivations of the CFT predictions for the entanglement Hamiltonians.

3. Interval in the infinite line

In this section we consider the harmonic chain on the infinite line and perform a numerical analysis to study the continuum limit of the entanglement Hamiltonian of an interval. We follow the procedure discussed in [20, 22] for the continuum limit of the entanglement Hamiltonian of an interval in the infinite chain of free fermions. In section 3.1 we introduce the two-point correlators to construct Q_A and P_A and in section 3.2 we report the main analysis, which leads to the CFT prediction (2), with the

weight function (3) and the energy density (6). The entanglement spectrum is explored in section 3.3.

3.1. Correlators

The two-point correlators $\langle \hat{q}_i \hat{q}_j \rangle$ and $\langle \hat{p}_i \hat{p}_j \rangle$ in the ground state of a finite harmonic chain made by $\mathcal{L}$ sites ($1 \leqslant i \leqslant \mathcal{L}$ in (8)) with periodic boundary conditions ($\hat{q}_1 = \hat{q}_{\mathcal{L}+1}$ and $\hat{p}_1 = \hat{p}_{\mathcal{L}+1}$) are respectively

$$\langle \hat{q}_i \hat{q}_j \rangle = \frac{1}{2\mathcal{L}} \sum_{k=1}^{\mathcal{L}} \frac{1}{m\tilde{\omega}_k} \cos[2\pi k\,(i-j)/\mathcal{L}] \qquad \langle \hat{p}_i \hat{p}_j \rangle = \frac{1}{2\mathcal{L}} \sum_{k=1}^{\mathcal{L}} m\tilde{\omega}_k \cos[2\pi k\,(i-j)/\mathcal{L}] \tag{21}$$

where the dispersion relation reads

$$\tilde{\omega}_k \equiv \sqrt{\omega^2 + \frac{4\kappa}{m} \left[\sin(\pi k/\mathcal{L}) \right]^2} \geqslant \omega \qquad 1 \leqslant k \leqslant \mathcal{L}. \tag{22}$$

The translation invariance induces the occurrence of the zero mode, that corresponds to $k = \mathcal{L}$. Since $\tilde{\omega}_{\mathcal{L}} = \omega$, it is straightforward to observe that $\langle \hat{q}_i \hat{q}_j \rangle$ diverges as $\omega \to 0$; hence the mass cannot be set to zero in the numerical analysis of this system.

In the thermodynamic limit $\mathcal{L} \to +\infty$, the correlators in (21) can be written as the integrals

$$\langle \hat{q}_i \hat{q}_j \rangle = \frac{1}{4\pi\,m} \int_0^{2\pi} \frac{\cos[\theta\,(i-j)]}{\sqrt{\omega^2 + (4\kappa/m) \left[\sin(\theta/2) \right]^2}} \, \mathrm{d}\theta \tag{23}$$

$$\langle \hat{p}_i \hat{p}_j \rangle = \frac{m}{4\pi} \int_0^{2\pi} \sqrt{\omega^2 + \frac{4\kappa}{m} \left[\sin(\theta/2) \right]^2} \, \cos[\theta\,(i-j)] \, \mathrm{d}\theta \tag{24}$$

which can be evaluated analytically, finding the following expressions in terms of the hypergeometric function [30]

$$\langle \hat{q}_i \hat{q}_j \rangle = \frac{\zeta^{i-j+1/2}}{2\sqrt{\kappa m}} \binom{i-j-1/2}{i-j} {}_2F_1\left(1/2\,, i-j+1/2\,, i-j+1, \zeta^2\right) \tag{25}$$

$$\langle \hat{p}_i \hat{p}_j \rangle = \frac{\sqrt{\kappa m}\,\zeta^{i-j-1/2}}{2} \binom{i-j-3/2}{i-j} {}_2F_1\left(-1/2\,, i-j-1/2\,, i-j+1, \zeta^2\right) \tag{26}$$

where the parameter ζ is defined as

$$\zeta \equiv \frac{\left(\omega - \sqrt{\omega^2 + 4\kappa/m}\right)^2}{4\kappa/m}. \tag{27}$$

The reduced correlation matrices Q_A and P_A are obtained by restricting the indices i and j of the correlators (25) and (26) to the interval A, i.e. to the integer values in $[1, L]$. By employing these reduced correlation matrices into (10), one finds the entanglement Hamiltonian matrix H_A. The entanglement Hamiltonian of the interval in the infinite line is obtained by plugging the matrix H_A into (9).

3.2. Entanglement Hamiltonian

The entanglement Hamiltonian of a block made by L consecutive sites in the infinite line, when the entire harmonic chain is in its ground state, is the operator constructed as explained in section 3.1. Considering the massless regime, we study the procedure to obtain the CFT prediction (2), with $\beta(x)$ and $T_{00}(x)$ given by (3) and (6) respectively, through a numerical analysis of the continuum limit.

The translation invariance of the entire system prevents us from setting $\omega = 0$ in our numerical analysis, as already remarked in section 3.1. The data reported in all the figures discussed in this subsection have been obtained for $\omega L = 10^{-500}$. The choice of this value is discussed in the appendix.

In figures 2 and 3 we show the data for the diagonals $M_{i,i+k}/L$ and $N_{i,i+k}/L$ with $0 \leqslant k \leqslant 7$ for some values of L. These numerical results lead us to conclude that the limits in (20) provide well-defined functions. Furthermore, these functions have a well-defined sign given by the parity of k, are symmetric under reflection with respect to the centre of the interval (we checked numerically that this symmetry holds also for the data points, i.e. that $M_{i,i+p} = M_{L-i-p+1,L-i+1}$ and $N_{i,i+p} = N_{L-i-p+1,L-i+1}$), and the absolute value of their maximum significantly decreases as k increases. It would be interesting to find analytic expressions for the functions defined through the limits (20), as done in [20] for the interval in the infinite chain of free fermions. In all the figures of this manuscript where some quantity has been plotted in terms of the spatial index, for the sake of simplicity we have written i on the horizontal axis instead of $i - 1/2$, which is the correct label corresponding to the data.

Assuming that the functions μ_k and ν_k introduced in (20) are well defined, let us study the continuum limit of the entanglement Hamiltonian (12), where the quadratic operators $\widehat{H}_M$ and $\widehat{H}_N$ have been introduced in (13). In the following we adapt the procedure discussed in [22] for the entanglement Hamiltonian of an interval in the infinite chain of free fermions. The quadratic operators $\widehat{H}_M$ and $\widehat{H}_N$ can be decomposed in different ways, as discussed in section 2 and in the appendix. For the sake of simplicity, in the following we describe the continuum limit for the decomposition given by (14) and (15), but the procedure can be easily adapted to the ones given by (16) and (17) or by (18) and (19). In the appendix we discuss another decomposition, inspired by the numerical analysis performed in [22].

The continuum limit is defined through the infinitesimal UV cutoff a: it corresponds to take $a \to 0$ and $L \to \infty$ while $La = \ell$ is kept constant. The position within the interval is labelled by $x = ia$ with $0 < x < \ell$. This leads us to write the independent variable in (20) as follows

$$x_k = \frac{x}{La} + \frac{ka/2}{La} \tag{28}$$

which tells us that $\mu_k = \mu_k(x + ka/2)$ and $\nu_k = \nu_k(x + ka/2)$.

In the continuum limit, the fields $\Phi(x)$ and $\Pi(x)$ are introduced through the position and momentum operators as follows [31]

$$\hat{q}_i \longrightarrow \Phi(x) \qquad \hat{p}_i \longrightarrow a\,\Pi(x) \tag{29}$$
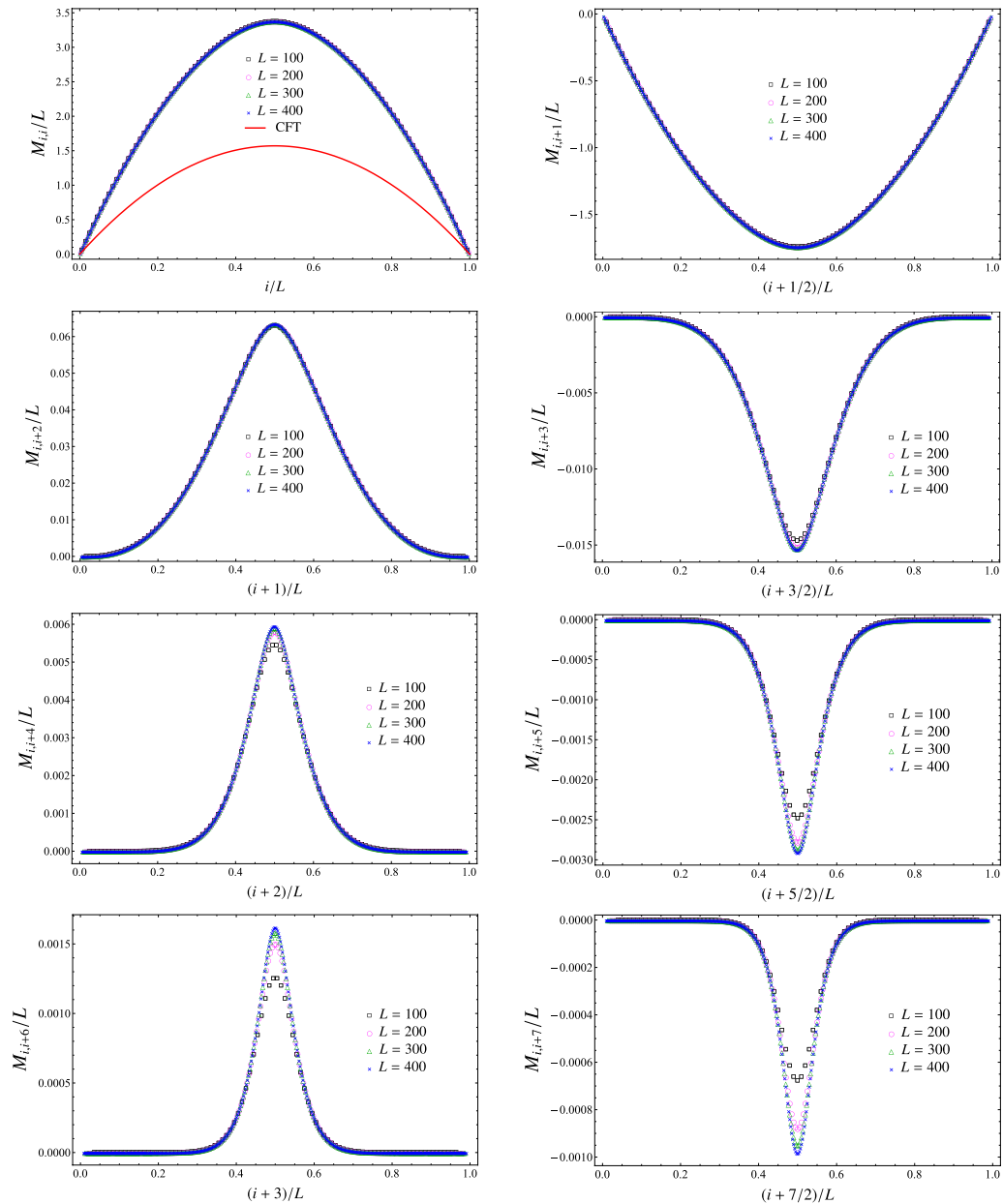
Figure 2. Diagonals of the matrix M (see (20)) when the subsystem is an interval made by L sites in the infinite line and $\omega L = 10^{-500}$. The red solid curve is the parabola (3).

where the UV cutoff guarantees that these fields satisfy the canonical commutation relations in the continuum limit, where the delta function occurs. The operators $\hat{q}_{i+k}$ and $\hat{p}_{i+k}$ in (14) and (15) lead to fields whose argument is properly shifted. By employing (29) and the Taylor expansion as $a \to 0$, in the continuum limit it is straightforward to obtain that

$$\hat{q}_{i+k} \;\longrightarrow\; \Phi(x + ka) = \sum_{p \geqslant 0} \frac{(ka)^p}{p!} \, \partial_x^p \Phi(x) \tag{30}$$
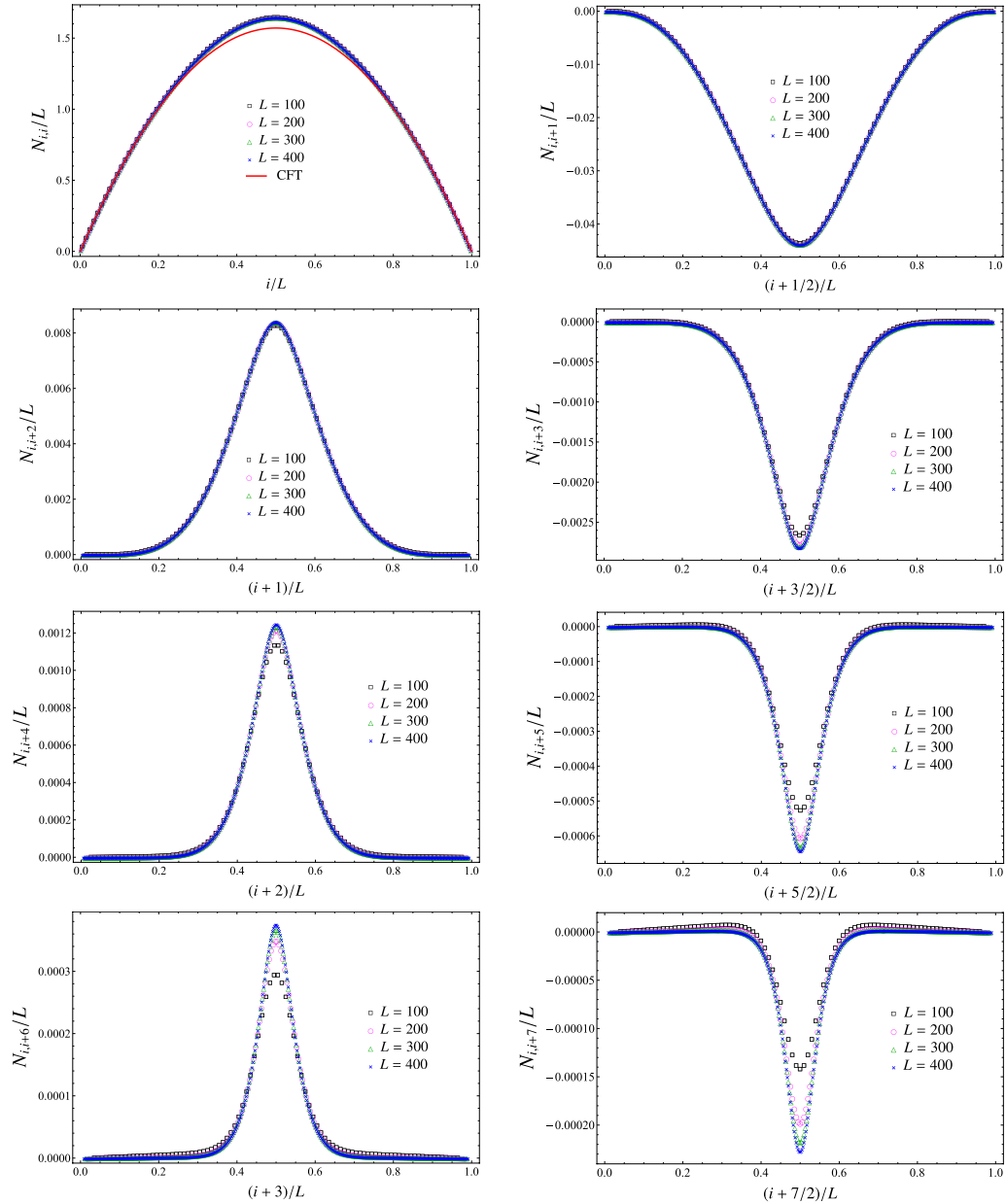
Figure 3. Diagonals of the matrix N (see (20)) when the subsystem is an interval made by L sites in the infinite line and $\omega L = 10^{-500}$. The red solid curve is the parabola (3).

and

$$\hat{p}_{i+k} \longrightarrow a\,\Pi(x + ka) = a \sum_{p \geqslant 0} \frac{(ka)^p}{p!}\,\partial_x^p \Pi(x). \tag{31}$$

In (14) and (15) we find it convenient to insert the UV cutoff into the sums by writing them as $L \sum_{i=1}^{L} (\dots) = \frac{(La)}{a^2} \sum_{i=1}^{L} (\dots)a$ because $\sum_{i=1}^{L} (\dots)a \longrightarrow \int_0^{\ell} (\dots)\mathrm{d}x$ in the continuum limit and the divergent factor L provides the factor ℓ. From (29)–(31), for

the operators (14) and (15) it is straightforward to obtain $\widehat{H}_M \longrightarrow H_M$ and $\widehat{H}_N \longrightarrow H_N$ respectively in the continuum limit, where

$$H_M = \frac{\ell}{a^2} \int_0^\ell \left(\mu_0(x)\,\Phi(x)^2 + 2\sum_{k=1}^{k_{\max}} \mu_k(x + ka/2)\,\Phi(x)\,\Phi(x + ka) \right) \mathrm{d}x \qquad (32)$$

$$H_N = \ell \int_0^\ell \left(\nu_0(x)\,\Pi(x)^2 + 2\sum_{k=1}^{k_{\max}} \nu_k(x + ka/2)\,\Pi(x)\,\Pi(x + ka) \right) \mathrm{d}x \qquad (33)$$

where $k_{\max}$ is the number of diagonals to include in the sums occurring in these expressions.

In our numerical analysis the parameter $k_{\max}$ plays a crucial role which is discussed below in this subsection and also in the appendix. Since $k_{\max} \to \infty$ in the continuum limit (see (30) and (31)), increasing values of $k_{\max}$ are considered. We find it worth remarking that the limit $L \to \infty$ in (20) is taken before the limit $k_{\max} \to \infty$. This implies that we have to consider the regime given by $k_{\max} \ll L$ in our numerical studies, where both L and $k_{\max}$ are finite.

Since $a \to 0$ in the continuum limit, we expand the integrands in (32) and (33) by keeping only the terms that could provide a non-vanishing contribution after the limit. For (32) we obtain

$$H_M = \frac{\ell}{a^2} \int_0^\ell \left\{ \mathcal{M}_{k_{\max}}^{(0)}(x)\,\Phi(x)^2 + a \sum_{k=1}^{k_{\max}} k \left[\mu_k'(x)\,\Phi(x) + 2\,\mu_k(x)\,\Phi(x)' \right] \Phi(x) \right.$$
$$\left. + a^2 \sum_{k=1}^{k_{\max}} k^2 \left[\frac{1}{4}\,\mu_k''(x)\,\Phi(x) + \partial_x\Big(\mu_k(x)\,\Phi'(x) \Big) \right] \Phi(x) \right\} \mathrm{d}x + O(a) \qquad (34)$$

where we have introduced the function

$$\mathcal{M}_{k_{\max}}^{(0)}(x) \equiv \lim_{L\to\infty} \frac{\mathsf{M}_{k_{\max}}^{(0)}(i)}{L} = \mu_0(x) + 2\sum_{k=1}^{k_{\max}} \mu_k(x) \qquad (35)$$

defined by combining the diagonals of the symmetric matrix M as follows

$$\mathsf{M}_{k_{\max}}^{(0)}(i) \equiv M_{i,i} + 2\sum_{k=1}^{k_{\max}} M_{i,i+k}. \qquad (36)$$

While the expansion (34) contains terms that are divergent if the corresponding weight functions are non-vanishing, it is straightforward to notice that (33) is finite as $a \to 0$. Indeed, its Taylor expansion reads

$$H_N = \ell \int_0^\ell \mathcal{N}_{k_{\max}}^{(0)}(x)\,\Pi(x)^2 \, \mathrm{d}x + O(a) \qquad (37)$$

where the function $\mathcal{N}_{k_{\max}}^{(0)}(x)$ is the combination of the functions $\nu_k(x)$ in (20) given by

$$\mathcal{N}_{k_{\max}}^{(0)}(x) \equiv \lim_{L\to\infty} \frac{\mathsf{N}_{k_{\max}}^{(0)}(i)}{L} = \nu_0(x) + 2\sum_{k=1}^{k_{\max}} \nu_k(x) \qquad (38)$$

where $\mathsf{N}^{(0)}_{k_{\max}}(i)$ is the same combination of the corresponding diagonals of the symmetric matrix N, namely

$$\mathsf{N}^{(0)}_{k_{\max}}(i) \equiv N_{i,i} + 2\sum_{k=1}^{k_{\max}} N_{i,i+k}. \tag{39}$$

Assuming that the integral and the discrete sums can be exchanged in the expression (34) for H_M, one notices that the integrand of the $O(1/a)$ term is the total derivative $\partial_x[\mu_k(x)\,\Phi(x)^2]$; hence its integration provides the boundary terms $[\mu_k(x)\,\Phi(x)^2]|_{x=0}^{x=\ell}$. These boundary terms vanish because $\mu_k(0) = \mu_k(\ell) = 0$ for the interval in the infinite line (see figure 2). As for the $O(1)$ term in (34), an integration by parts can be performed for the term whose integrand is $\Phi(x)\,\partial_x[\mu_k(x)\,\Phi(x)']$, and the resulting boundary terms vanish, again because $\mu_k(0) = \mu_k(\ell) = 0$. By employing these observations and discarding the $O(a)$ terms, the expression (34) can be written as follows

$$H_M = \frac{\ell}{a^2}\int_0^\ell \left\{ \mathcal{M}^{(0)}_{k_{\max}}(x)\,\Phi(x)^2 + a^2\sum_{k=1}^{k_{\max}} k^2\left[\frac{1}{4}\,\mu_k''(x)\,\Phi(x)^2 - \mu_k(x)\left(\Phi'(x)\right)^2\right]\right\}\mathrm{d}x. \tag{40}$$

Considering the integral whose integrand is $\mu_k(x)[\Phi'(x)]^2$ from the $O(1)$ term of this expression, we find it worth defining

$$\mathcal{M}^{(2)}_{k_{\max}}(x) \equiv \lim_{L\to\infty} \frac{\mathsf{M}^{(2)}_{k_{\max}}(i)}{L} \equiv \sum_{k=1}^{k_{\max}} k^2\mu_k(x_k) \tag{41}$$

where, by using (20), we have introduced the following combination of diagonals of the symmetric matrix M

$$\mathsf{M}^{(2)}_{k_{\max}}(i) \equiv \sum_{k=1}^{k_{\max}} k^2 M_{i,i+k}. \tag{42}$$

As for the integral whose integrand is $\mu_k''(x)\,\Phi(x)^2$ in (40), we approximate the functions $\mu_k''(x)$ through finite differences because the analytic expressions of the functions $\mu_k(x)$ are not available. Thus, we have

$$a^2\mu_k''(x) = \mu_k(x+a) - 2\,\mu_k(x) + \mu_k(x-a). \tag{43}$$

This expression and (20) naturally lead us to introduce

$$\mathcal{M}^{(2)}_{2,k_{\max}}(x) \equiv \lim_{L\to\infty} \frac{\mathsf{M}^{(2)}_{2,k_{\max}}(i)}{L} \equiv \sum_{k=1}^{k_{\max}} k^2\mu_{2,k}(x_k) \tag{44}$$

where the subindex 2 indicates that these quantities are related to the second derivative of $\mu_k(x)$. In (44) we have defined the functions $\mu_{2,k}(x_k)$ as follows

$$\lim_{L\to\infty} \frac{M_{i+1,i+1+k} - 2M_{i,i+k} + M_{i-1,i-1+k}}{L} \equiv \mu_{2,k}(x_k) \tag{45}$$

and the combinations of matrix elements of M given by

$$\mathsf{M}^{(2)}_{2,k_{\max}}(i) \equiv \sum_{k=1}^{k_{\max}} k^2 \big(M_{i+1,i+1+k} - 2M_{i,i+k} + M_{i-1,i-1+k} \big). \tag{46}$$

In the continuum limit $k_{\max} \to \infty$; hence we introduce the weight functions obtained by taking this limit in (35), (38), (41) and (44), namely

$$\mathcal{M}^{(0)}_{k_{\max}}(x) \longrightarrow \mathcal{M}^{(0)}_{\infty}(x) \qquad\qquad \mathcal{N}^{(0)}_{k_{\max}}(x) \longrightarrow \mathcal{N}^{(0)}_{\infty}(x) \tag{47}$$

and

$$\mathcal{M}^{(2)}_{k_{\max}}(x) \longrightarrow \mathcal{M}^{(2)}_{\infty}(x) \qquad\qquad \mathcal{M}^{(2)}_{2,k_{\max}}(x) \longrightarrow \mathcal{M}^{(2)}_{2,\infty}(x). \tag{48}$$

Summarising, the continuum limit of the entanglement Hamiltonian (12) obtained from (14) and (15) is found by taking the limit $k_{\max} \to \infty$ of half of the sum of (37) and (40). By employing the functions introduced in (47) and (48), for the continuum limit of the entanglement Hamiltonian (12) we find

$$
\begin{aligned}
\frac{H_M + H_N}{2} = {} & \frac{\ell}{a^2} \int_0^\ell \frac{1}{2} \left[\mathcal{M}^{(0)}_{\infty}(x) + \frac{1}{4} \mathcal{M}^{(2)}_{2,\infty}(x) \right] \Phi(x)^2 \, \mathrm{d}x \\
& + \ell \int_0^\ell \frac{1}{2} \Big[\mathcal{N}^{(0)}_{\infty}(x) \, \Pi(x)^2 - \mathcal{M}^{(2)}_{\infty}(x) \big(\Phi'(x) \big)^2 \Big] \mathrm{d}x + O(a).
\end{aligned}
\tag{49}
$$

Since analytical results for the functions μ_k and ν_k are not available, we study the weight functions $\mathcal{M}^{(0)}_{\infty}(x)$, $\mathcal{M}^{(2)}_{2,\infty}(x)$, $\mathcal{N}^{(0)}_{\infty}(x)$ and $\mathcal{M}^{(2)}_{\infty}(x)$ in (49) by performing a numerical analysis of the combinations of the matrix elements of M and N defining them, which are given respectively by (36), (46), (39) and (42). These combinations depend on the number of sites L in the interval and on the parameter $k_{\max}$ labelling the number of diagonals to include in the sums. As already remarked above, we study the continuum limit by taking $L \to \infty$ first, in order to guarantee that the functions μ_k and ν_k in (20) are well defined, and then $k_{\max} \to \infty$. This means that we must keep $k_{\max} \ll L$ in our numerical analysis. If we had analytic expressions for the functions μ_k and ν_k, we could check whether they vanish fast enough as $k \to \infty$ to find convergence in the infinite sums defining the weight functions in (47) and (48), which occur in (49).

It is important to observe that, since (36), (39), (46) and (42) can be evaluated only in the spatial range given by $1 \leqslant i \leqslant L - k_{\max}$, these combinations are not defined on the whole interval for finite values of L and $k_{\max}$. The numerical results for these combinations are shown in the appendix (see the top panels in figures A2 and A3): they do not provide symmetric curves with respect to the centre of the interval, as expected from the symmetry of the configuration, and they do not capture the CFT curve close to the right endpoint of the interval. This motivates us to employ decompositions of the operators $\widehat{H}_M$ and $\widehat{H}_N$ that are more suitable than (14) and (15) to obtain the CFT predictions on the entire interval. The decompositions (16) and (17) provide curves that are symmetric with respect to the centre of the interval, but they do not allow us to recover the CFT curve close to both the endpoints of the interval (see the middle panels in figures A2 and A3). In the following we consider the decompositions (18) and (19).

The procedure explained above to study the continuum limit of the entanglement Hamiltonian can be adapted straightforwardly to the case where the decompositions

(18) and (19) are employed. The result is again (49), with the weight functions given by (47) and (48). The crucial difference with respect to the previous analysis is that, as $L \to \infty$, in (47) we have $\mathsf{M}_{k_{\max}}^{(0)}(i)/L \to \mathcal{M}_{k_{\max}}^{(0)}(x)$ with

$$\mathsf{M}_{k_{\max}}^{(0)}(i) = \begin{cases} M_{i,i} + 2\sum_{k=1}^{k_{\max}} M_{i,i+k} & 1 \leqslant i \leqslant L/2 \\ M_{i,i} + 2\sum_{k=1}^{k_{\max}} M_{i-k,i} & L/2+1 \leqslant i \leqslant L \end{cases} \tag{50}$$

and $\mathsf{N}_{k_{\max}}^{(0)}(i)/L \to \mathcal{N}_{k_{\max}}^{(0)}(x)$ with

$$\mathsf{N}_{k_{\max}}^{(0)}(i) = \begin{cases} N_{i,i} + 2\sum_{k=1}^{k_{\max}} N_{i,i+k} & 1 \leqslant i \leqslant L/2 \\ N_{i,i} + 2\sum_{k=1}^{k_{\max}} N_{i-k,i} & L/2+1 \leqslant i \leqslant L \end{cases} \tag{51}$$

while in (48) we have $\mathsf{M}_{k_{\max}}^{(2)}(i)/L \to \mathcal{M}_{k_{\max}}^{(2)}(x)$ with

$$\mathsf{M}_{k_{\max}}^{(2)}(i) = \begin{cases} \sum_{k=1}^{k_{\max}} k^2 M_{i,i+k} & 1 \leqslant i \leqslant L/2 \\ \sum_{k=1}^{k_{\max}} k^2 M_{i-k,i} & L/2+1 \leqslant i \leqslant L \end{cases} \tag{52}$$

and $\mathsf{M}_{2,k_{\max}}^{(2)}(i)/L \to \mathcal{M}_{2,k_{\max}}^{(2)}(x)$ with

$$\mathsf{M}_{2,k_{\max}}^{(2)}(i) = \begin{cases} \sum_{k=1}^{k_{\max}} k^2 \big(M_{i+1,i+1+k} - 2M_{i,i+k} + M_{i-1,i-1+k}\big) & 1 \leqslant i \leqslant L/2 \\ \sum_{k=1}^{k_{\max}} k^2 \big(M_{i-k+1,i+1} - 2M_{i-k,i} + M_{i-k-1,i-1}\big) & L/2+1 \leqslant i \leqslant L. \end{cases} \tag{53}$$

The occurrence of two branches in these functions of the spatial index i (which originates from the splitting of the range $1 \leqslant i \leqslant L$ in (18) and (19)) guarantees that they are well defined on the entire interval for finite values of $k_{\max} \ll L$. The combinations of diagonals in (50)–(53) display the symmetry under reflection with respect to the centre of the interval, which has been observed also for the diagonals of M and N (see figures 2 and 3).

In figure 4 we show some numerical results for the combinations in (50) and (53). From the left panel we observe that, when $k_{\max}$ is large enough, $\mathsf{M}_{k_{\max}}^{(0)}$ converges to a well-defined function of $x/\ell \in (0,1)$. This observation allows us to conclude that $\mathsf{M}_{k_{\max}}^{(0)}/L \to 0$ as $L \to \infty$ at any given value of $x/\ell \in (0,1)$. Similarly, the data reported in the right panel of figure 4 show that, when $k_{\max}$ is large enough, the product $L\,\mathsf{M}_{2,k_{\max}}^{(2)}$ for increasing values of L collapses on the horizontal line corresponding to 4π except for four isolated and finite picks in each curve, whose positions depend on L and whose heights are independent of L. The positions of these picks are symmetric with respect to the centre of the interval and they move towards the centre of the interval as L increases. These observations allow us to conclude that $\mathsf{M}_{2,k_{\max}}^{(2)}/L \to 0$ as $L \to \infty$. Thus, the collapses of the data points observed in figure 4 for increasing values of L lead us to conclude that for the weight functions occurring in the $O(1/a^2)$ term of (49) we should have

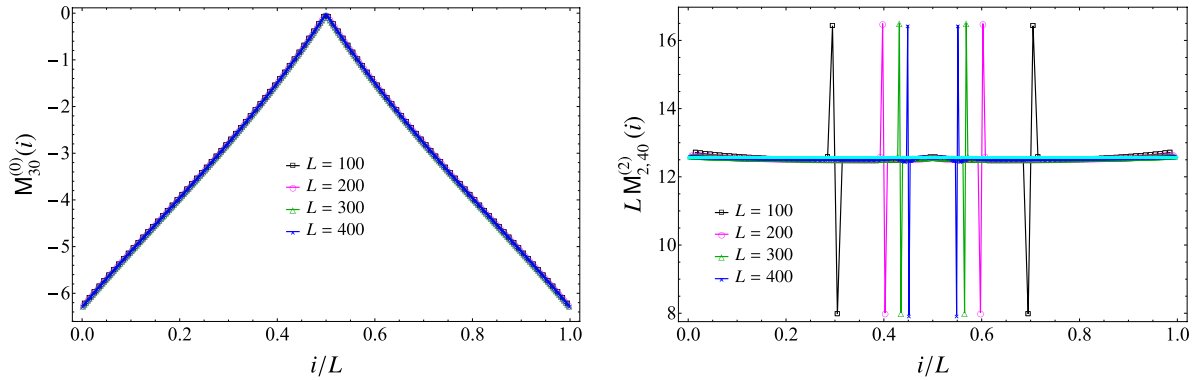$$\mathcal{M}_{\infty}^{(0)}(x) = 0 \qquad \mathcal{M}_{2,\infty}^{(2)}(x) = 0. \tag{54}$$

Figure 4. The combinations (50) (left) and (53) (right) when the subsystem is an interval made by L sites in the infinite line and $\omega L = 10^{-500}$. The cyan horizontal line in the right panel corresponds to 4π. The collapses of the data points for increasing values of L support (54).

The curves in figure 4 are obtained through the decompositions (18) and (19). Considering the other decompositions reported in section 2 and in the appendix, one finds different curves, but all of them lead to the CFT prediction (54).

In figures 5 and 6 we report numerical results for the combinations in (51) and (52). Comparing these two figures, it is straightforward to conclude that the agreement between the numerical data and the CFT prediction $\beta(x)$ given by the parabola (3) (red solid curve) improves as $k_{\max} \ll L$ increases, i.e. by including more diagonals in the sums occurring in (51) and (52). The data reported in figures 4 and 5 correspond to the optimal values of $k_{\max}$, when the behaviours of the data become stable. These optimal values are different for the combinations involving M and N. From figure 6 we also observe a parity effect in $k_{\max}$: the asymptotic curve for a given $k_{\max}$ is either above or below the CFT curve, depending on the parity of $k_{\max}$, and the distances between these curves decrease as $k_{\max}$ increases until the optimal value is reached. This parity effect in $k_{\max}$ is due to the fact that the kth diagonals of M and N (i.e. $M_{i,i+k}$ and $N_{i,i+k}$ for a given k) have a definite sign determined by the parity of k (see figures 2 and 3) and that $\mathsf{M}^{(2)}_{k_{\max}}$ and $\mathsf{N}^{(0)}_{k_{\max}}$ are linear combinations of these diagonals through positive coefficients.

We remark that the data points reported in figures 4–6 probe the entire interval A, including the neighbourhoods of the endpoints. Furthermore, the resulting curves are symmetric under reflection with respect to the centre of the interval, as expected for this bipartition. These features support our choice to employ the combinations (50)–(53).

The collapses of the data points in figure 5 for increasing values of L lead to the conjecture that the weight functions occurring in the finite term of (49) are

$$\mathcal{M}^{(2)}_{\infty}(x) = -\beta(x) \qquad \qquad \mathcal{N}^{(0)}_{\infty}(x) = \beta(x). \qquad (55)$$

Thus, by employing the numerical results (54) and (55) in the expression (49) for the entanglement Hamiltonian of an interval in the infinite line, we find the CFT prediction (2) with $\beta(x)$ given by (3) and the energy density by (6).

We find it worth remarking that the height of the cyan horizontal line in the right panel of figure 4 corresponds to $4\pi = -\ell^2 \beta(x)''$, with $\beta(x)$ being the weight function (3) predicted by CFT. A naive explanation of this observation comes from the fact that
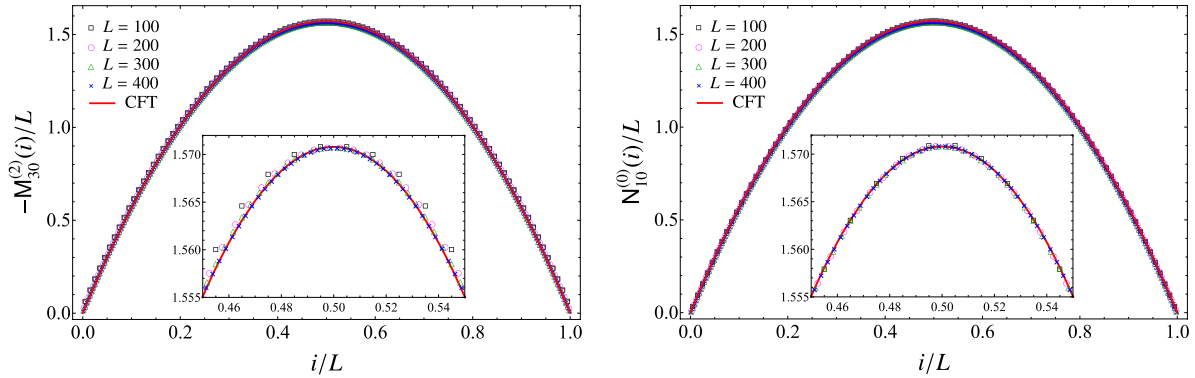
Figure 5. The combinations (52) (left) and (51) (right) when the subsystem is an interval made by L sites in the infinite line and $\omega L = 10^{-500}$. The collapses of the data points corresponding to increasing values of L support (55), with $\beta(x)$ given by the parabola (3) (red solid curve).

$\mathsf{M}^{(2)}_{2,k_{\max}}$ is a combination obtained through a finite differences approximation of $\mu''_k(x)$ (see (46)) and that the combination $\mathsf{M}^{(2)}_{k_{\max}}$ of $\mu_k(x)$ provides $-\beta(x)$ in the continuum limit (see (55)). Nonetheless, an exchange of the second derivate of $\mu_k(x)$ with the discrete sum over k in (34) would provide an unexpected term containing Φ^2 multiplied by a constant weight function in the entanglement Hamiltonian. This leads us to conclude that exchanges between derivatives with respect to x and discrete sums over k are not allowed.

3.3. Entanglement spectrum

In a two-dimensional CFT, the entanglement spectra of an interval for the bipartitions shown in figure 1 have been studied in [13] through methods of BCFT [25, 32, 33]. The occurrence of boundaries is due to the regularisation procedure, as briefly mentioned in section 1. In the imaginary time description of the two-dimensional spacetime underlying the bipartitions shown in figure 1, the UV cutoff ϵ can be introduced by removing an infinitesimal disk of radius ϵ around each entangling point [7, 13, 18, 24]. For the interval in the infinite line (left panel of figure 1), the remaining spacetime has two boundaries which encircle the two endpoints of the interval A; hence it can be mapped into an annulus through a conformal transformation. Given the symmetry of this bipartition with respect to the centre of the interval, the same conformal boundary condition must be imposed on the two boundaries.

For harmonic chains in Gaussian states, standard techniques allow us to evaluate the entanglement spectrum in terms of the single-particle entanglement energies ε_r, which are obtained from the symplectic spectrum of the reduced covariance matrix of the subsystem [1, 2, 17, 27, 34]. Once the single-particle entanglement energies have been ordered as $\varepsilon_1 \leqslant \varepsilon_2 \leqslant \cdots \leqslant \varepsilon_L$, the gaps g_r introduced in section 1 can be written as linear combinations $\sum_{k=1}^{L} n_k \varepsilon_k$ with non-negative integer coefficients n_k.

In the top left panel of figure 7, we report some numerical results for ε_1. For a given finite value of L, we observe that $\varepsilon_1 \to 0$ as $\omega L \to 0$, while this does not happen for ε_r with $r > 1$. This leads us to assume that ε_1 vanishes in the comparison of the numerical
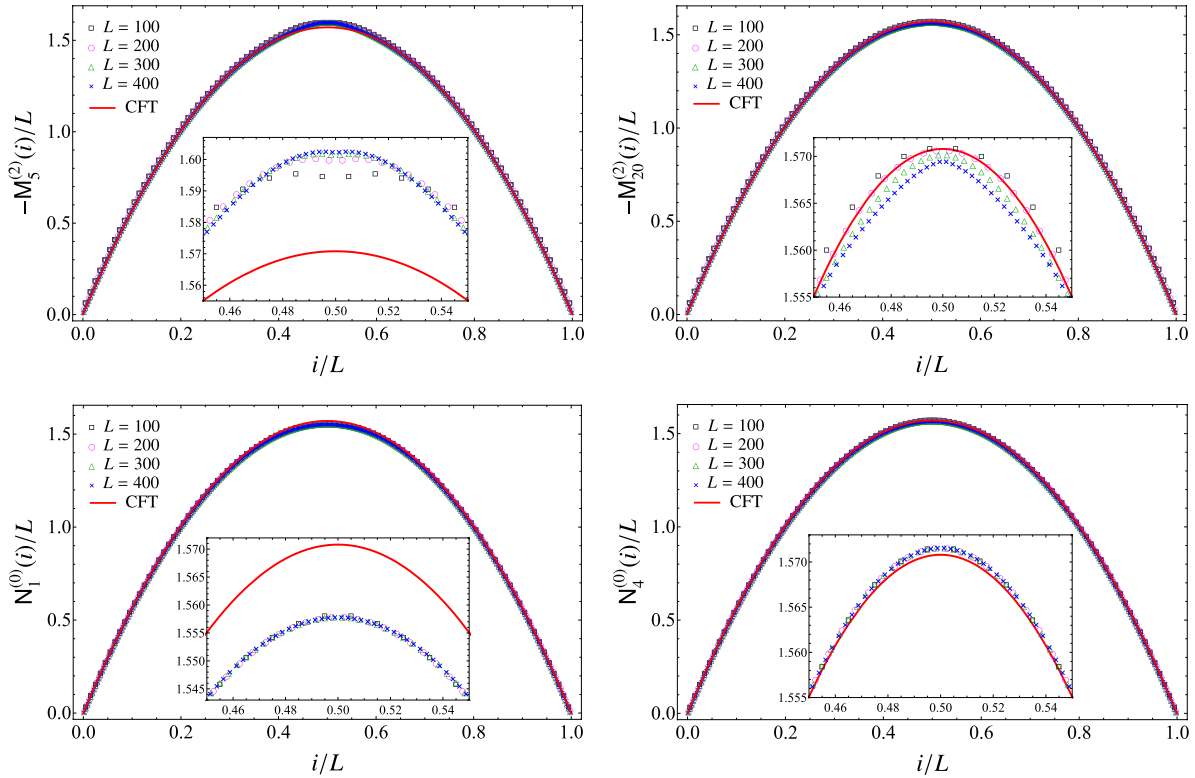
Figure 6. Role of the parameter k_{max} in the combinations (52) (top panels) and (51) (bottom panels) when the subsystem is an interval made by L sites in the infinite line and $\omega L = 10^{-500}$. The insets, which zoom in on the central part of the interval, show that the agreement with the CFT prediction given by the parabola (3) (red solid curve) improves as k_{max} increases.

data with the CFT predictions in the bottom panel of figure 7. In the top right panel of figure 7 we show the single-particle entanglement energies ε_k/L in terms of k/L for some values of L and, if L is large enough, we find that the data having different L collapse on a well-defined curve, that would be interesting to obtain analytically. Given the above assumption about ε_1, in the bottom panel of figure 7 we show the numerical data for the ratios g_r/g_1 of the gaps with respect to the first gap as functions of $\log L$. It is remarkable to observe that, as L increases, the values of g_r/g_1 with $1 \leqslant r \leqslant 29$ collapse on all the integers n with $1 \leqslant n \leqslant 6$ (we checked that $g_r/g_1 > 6.5$ when $r \geqslant 30$ for the largest value of L at our disposal). This originates from the fact that the single-particle entanglement energies in the low-lying part of the spectrum are equally separated by a multiple integer of ε_2. Furthermore, the degeneracy of the nth level is given by the number of possible ways to partition the integer n. This happens because in this model the low-lying part of the single-particle entanglement spectrum contains the first positive integer numbers once the normalisation through ε_2 is introduced.

These numerical results for g_r/g_1 are compatible with the conformal spectrum of the BCFT given by a free massless scalar field on the segment with either Dirichlet or Neumann boundary conditions imposed on both the endpoints of the segment [33, 35], but they cannot discriminate between these two possibilities. As discussed e.g. in [33], when the same boundary conditions are imposed on both the boundaries,
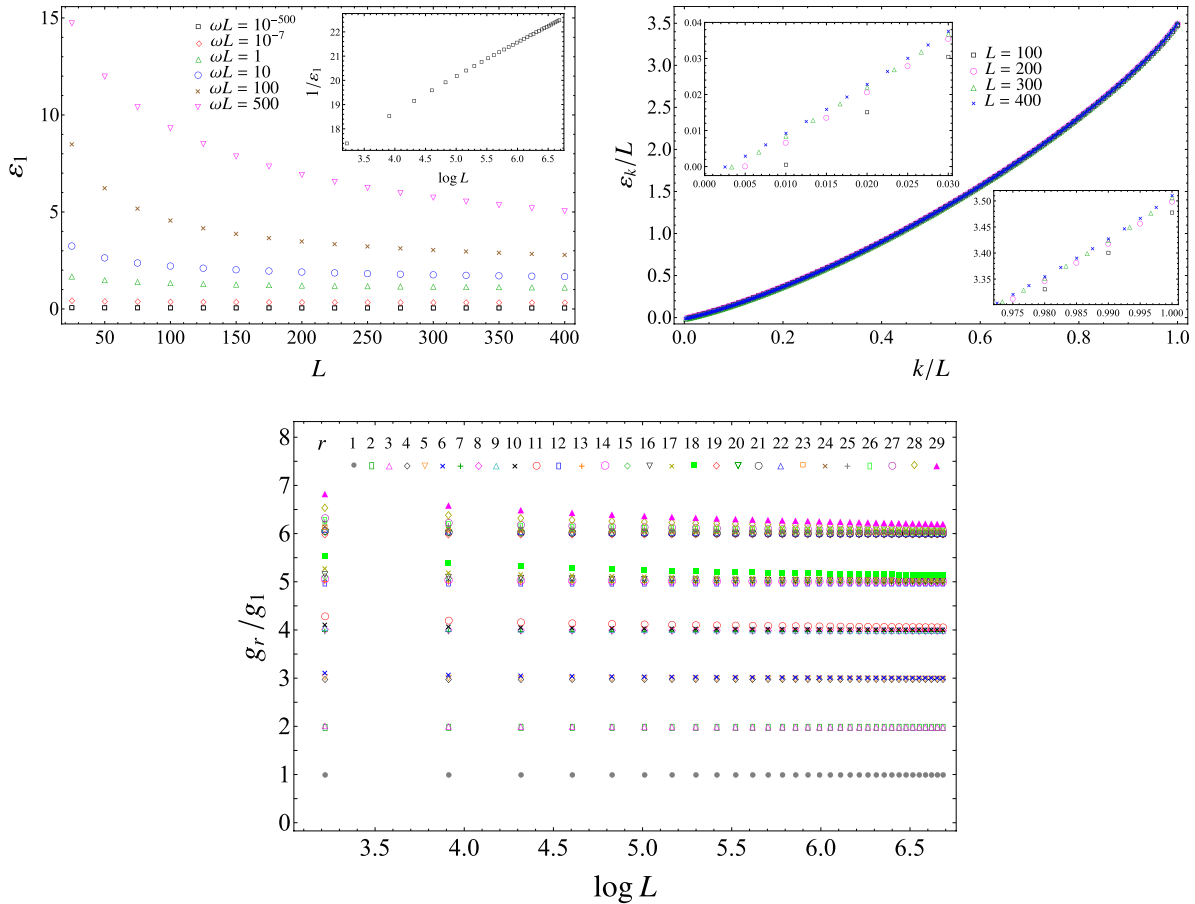
Figure 7. Entanglement spectrum for an interval in the infinite line. Top left: the smallest single-particle entanglement energy ε_1 as a function of the number of sites L of the interval, for increasing values of ωL. Top right: the single-particle entanglement energies ε_k for different values of L (the insets zoom in on the lowest and highest values of k). Bottom: the ratios of the gaps g_r in the entanglement spectrum as functions of $\log L$ in the massless regime, i.e. when $\omega L = 10^{-500}$.

the Laurent expansion of the holomorphic part of the primary field $\partial_z \Phi(z)$ reads $\partial_z \Phi(z) = \sum_{n \in \mathbb{Z}} j_n J_n(z)$, being z the complex variable in Euclidean signature and where it is worth remarking that the index of the sum runs over the integer numbers. The functions $J_n(z)$ form an orthonormal basis and their explicit expressions depend on whether Neumann or Dirichlet boundary conditions are imposed. Since the Laurent modes satisfy the algebra $[j_m, j_n] = m\, \delta_{m+n,0}$ in the proper normalisation, the ground state $|0\rangle$ can be introduced in such a way that $j_n|0\rangle = 0$ for $n \geqslant 0$ and the Hilbert space can be constructed by acting with j_n, with $n < 0$ on the ground state. The conformal dimension of the field associated with the state $j_{-n_1} \ldots j_{-n_k}|0\rangle$ is $\sum_{l=1}^{k} n_l$ and this implies that the conformal spectrum contains the non-negative integer numbers, and the degeneracy of the level with dimension n is given by the number of ways to write n as a sum of integers.

The ambiguity between Neumann and Dirichlet boundary conditions can be resolved by considering the entanglement spectrum of an interval at the beginning of a semi-infinite line with Dirichlet boundary conditions, which will be discussed in section 4.3.

In terms of the primary fields and of their descendants, we observe the towers of the identity and of $\partial\Phi$.

The agreement found above with the spectrum of the BCFT of the free massless scalar field is expected only for the low-lying part of the entanglement spectrum.

4. Interval at the beginning of the semi-infinite line with Dirichlet boundary conditions

In this section we study the continuum limit of the entanglement Hamiltonian of L consecutive sites at the beginning of the massless harmonic chain on the semi-infinite line with Dirichlet boundary conditions at its endpoint. In section 4.1 we find analytic expressions for the two-point correlators at a generic value of the mass parameter. Focussing on the massless regime, in section 4.2 we adapt the procedure explained in section 3 to this case, finding the CFT prediction (2), with the weight function (4) and the energy density (7). The continuum limit of the entanglement spectrum is discussed in section 4.3.

4.1. Correlators

A finite harmonic chain in a segment with Dirichlet boundary conditions imposed at the endpoints is defined by (8) and by $\hat{q}_0 = \hat{q}_{\mathcal{L}} = \hat{p}_0 = \hat{p}_{\mathcal{L}} = 0$. The two-point correlators $\langle \hat{q}_i \hat{q}_j \rangle$ and $\langle \hat{p}_i \hat{p}_j \rangle$ in the ground state read respectively [36]

$$\langle \hat{q}_i \hat{q}_j \rangle = \frac{1}{\mathcal{L}} \sum_{k=1}^{\mathcal{L}-1} \frac{1}{m \tilde{\omega}_k} \, \sin(\pi k \, i / \mathcal{L}) \, \sin(\pi k \, j / \mathcal{L}) \tag{56}$$

$$\langle \hat{p}_i \hat{p}_j \rangle = \frac{1}{\mathcal{L}} \sum_{k=1}^{\mathcal{L}-1} m \tilde{\omega}_k \, \sin(\pi k \, i / \mathcal{L}) \, \sin(\pi k \, j / \mathcal{L}) \tag{57}$$

where the dispersion relation is

$$\tilde{\omega}_k \equiv \sqrt{\omega^2 + \frac{4\kappa}{m} \big[\sin(\pi k / (2\mathcal{L})) \big]^2} > \omega \qquad 1 \leqslant k \leqslant \mathcal{L} - 1. \tag{58}$$

In contrast with the harmonic chain in the infinite line (see section 3.1), this harmonic chain is not translation-invariant; hence the zero mode does not occur and the massless limit $\omega \to 0$ is well defined because the correlators (56) and (57) are finite.

In the thermodynamic limit, the correlators (56) and (57) can be written respectively as follows

$$\langle \hat{q}_i \hat{q}_j \rangle = \frac{1}{\pi \, m} \int_0^\pi \frac{\sin(\theta \, i) \, \sin(\theta \, j)}{\sqrt{\omega^2 + (4\kappa/m) \big[\sin(\theta/2) \big]^2}} \, \mathrm{d}\theta \tag{59}$$

$$\langle \hat{p}_i \hat{p}_j \rangle = \frac{m}{\pi} \int_0^\pi \sqrt{\omega^2 + \frac{4\kappa}{m} \left[\sin(\theta/2) \right]^2} \, \sin(\theta\,i)\,\sin(\theta\,j)\,\mathrm{d}\theta \tag{60}$$

where $i, j \geqslant 0$ and the Dirichlet boundary conditions are satisfied at the beginning of the semi-infinite line. We can evaluate the integrals (59) and (60) analytically by employing a prosthaphaeresis formula and an integral representation of the hypergeometric function[1]. The final result reads

$$\langle \hat{q}_i \hat{q}_j \rangle = \frac{1}{m\omega\,\sqrt{1+\kappa_\omega}} \left\{ F_+(|i-j|) - F_+(i+j) \right\} \tag{61}$$

$$\langle \hat{p}_i \hat{p}_j \rangle = m\omega\,\sqrt{1+\kappa_\omega} \left\{ F_-(|i-j|) - F_-(i+j) \right\} \tag{62}$$

where the functions $F_\pm(n)$ are defined as follows

$$F_\pm(n) \equiv \left(\frac{2(1+\kappa_\omega)}{\kappa_\omega} \right)^{\pm 1/2} \frac{\Gamma(n \pm 1/2)\,\zeta^{n\pm 1/2}}{n!\,2\,\Gamma(\pm 1/2)} \, {}_2F_1\big(\pm 1/2\,, n \pm 1/2\,, n+1, \zeta^2 \big) \tag{63}$$

with $\kappa_\omega \equiv 2\kappa/(m\omega^2)$ and ζ given by (27).

In the massless regime, which corresponds to $\omega = 0$, the expressions (61) and (62) significantly simplify and become the correlators found in [37], which are written in terms of the digamma function $\psi(z)$ respectively as

$$\langle \hat{q}_i \hat{q}_j \rangle = \frac{1}{2\pi\,\sqrt{\kappa m}} \Big(\psi(1/2 + i + j) - \psi(1/2 + i - j) \Big) \tag{64}$$

$$\langle \hat{p}_i \hat{p}_j \rangle = \frac{2\,\sqrt{\kappa m}}{\pi} \left(\frac{1}{4(i+j)^2 - 1} - \frac{1}{4(i-j)^2 - 1} \right). \tag{65}$$

By restricting the indices i and j of the correlators (64) and (65) to the interval A at the beginning of the semi-infinite line (see the right panel of figure 1), i.e. to the integer values in $[1, L]$, we get the reduced correlation matrices Q_A and P_A to employ in the expression (10) for the entanglement Hamiltonian matrix H_A. Plugging this matrix into (9), we can obtain the entanglement Hamiltonian of the interval A at the beginning of the semi-infinite line with Dirichlet boundary conditions imposed at its origin.

4.2. Entanglement Hamiltonian

We are interested in the bipartition of the semi-infinite line whose origin coincides with the left endpoint of the interval A made by L sites (see the right panel of figure 1), when the entire system is in its ground state. The entanglement entropy of this bipartition has been studied for various systems e.g. in [8, 38]. In the massless harmonic chain with

---

[1] The following integral representation for the hypergeometric function has been employed

$$\int_0^\pi \frac{\cos(n\theta)}{2\pi(1 - a\cos\theta)^b} \, \mathrm{d}\theta = \frac{2^{b-1}\,\Gamma(n+b)}{n!\,a^b\,\Gamma(b)} \left(\frac{1 - \sqrt{1-a^2}}{a} \right)^{n+b} {}_2F_1\left(b, n+b; n+1; \left(\frac{1 - \sqrt{1-a^2}}{a} \right)^2 \right)$$

in the special case given by $a = 2\zeta/(1+\zeta^2)$ and $b = \pm 1/2$.

21

Dirichlet boundary conditions, the entanglement Hamiltonian $\widehat{K}_A = (\widehat{H}_M + \widehat{H}_N)/2$ of this interval is given by (9) and (10), where the $L \times L$ matrices Q_A and P_A are the reduced correlation matrices introduced in section 4.1 through the correlators (64) and (65). The result for the continuum limit predicted by CFT is (2), with the weight function $\beta(x)$ given by (4) and the energy density (7) [29]. In the following we discuss a numerical procedure to obtain this CFT result.

The decompositions of the operators $\widehat{H}_M$ and $\widehat{H}_N$ introduced in section 2 and in the appendix naturally lead us to consider the kth diagonals of the symmetric matrices M and N, like in the case of the interval in the infinite line discussed in section 3.2. In the massless regime, we find numerical evidence that the limiting procedures defined in (20) provide well-defined functions for any given value of k. This is shown in figures 8 and 9 for the kth diagonal of the matrices M and N, respectively, with $0 \leqslant k \leqslant 7$. Notice that, while the functions μ_k and ν_k vanish at the entangling point that separates A and B, they are non-vanishing at the beginning of the semi-infinite line, where the Dirichlet boundary condition is imposed. It would be interesting to find analytic expressions for these functions. Like for the interval in the infinite line, these functions have a well-defined sign given by the parity of k and the absolute value of their maximum significantly decreases as k increases.

Assuming the existence of the functions μ_k and ν_k defined in (20), the continuum limit of the entanglement Hamiltonian (12) can be studied by adapting to the bipartition that we are considering the procedure described in section 3. Special care must be devoted to the boundary terms due to the integrations of a total derivative or to the integrations by parts. In particular, in (34) the integrand of the $O(1/a)$ term is the total derivative $\partial_x[\mu_k(x)\,\Phi(x)^2]$, whose integral over the interval gives the boundary terms $[\mu_k(x)\,\Phi(x)^2]|_{x=0}^{x=\ell}$. These boundary terms vanish because $\mu_k(\ell) = 0$ at the entangling point and the Dirichlet boundary condition $\Phi(0) = 0$ is imposed at the beginning of the semi-infinite line, where $\mu_k(0) \neq 0$. The remaining expression reads

$$H_M = \frac{\ell}{a^2} \int_0^\ell \mathcal{M}_{k_{\max}}^{(0)}(x)\,\Phi(x)^2\,\mathrm{d}x$$
$$+ \ell \int_0^\ell \sum_{k=1}^{k_{\max}} k^2 \left[\frac{1}{4}\,\mu_k''(x)\,\Phi(x) + \mu_k'(x)\,\Phi'(x) + \mu_k(x)\,\Phi''(x) \right] \Phi(x)\,\mathrm{d}x \tag{66}$$

where $O(a)$ terms have been discarded and $\mathcal{M}_{k_{\max}}^{(0)}(x)$ has been introduced in (35).

The $O(1)$ term in (66) is similar to the $O(1)$ term in (34) and the terms containing $\mu_k''(x)$ and $\mu_k(x)$ can be treated as discussed in section 3.2. As for the term whose integrand is $\mu_k'(x)\,\Phi'(x)\,\Phi(x)$, we approximate $\mu_k'(x)$ through finite differences by writing $\mu_k'(x) = [\mu_k(x + a) - \mu_k(x)]/a$ because analytic expressions for $\mu_k(x)$ are not known. Combining this approximation with (20) and (66), we are naturally led to introduce

$$\mathsf{M}_{1,k_{\max}}^{(2)}(i) \equiv \sum_{k=1}^{k_{\max}} k^2 \big(M_{i+1,i+1+k} - M_{i,i+k}\big) \tag{67}$$
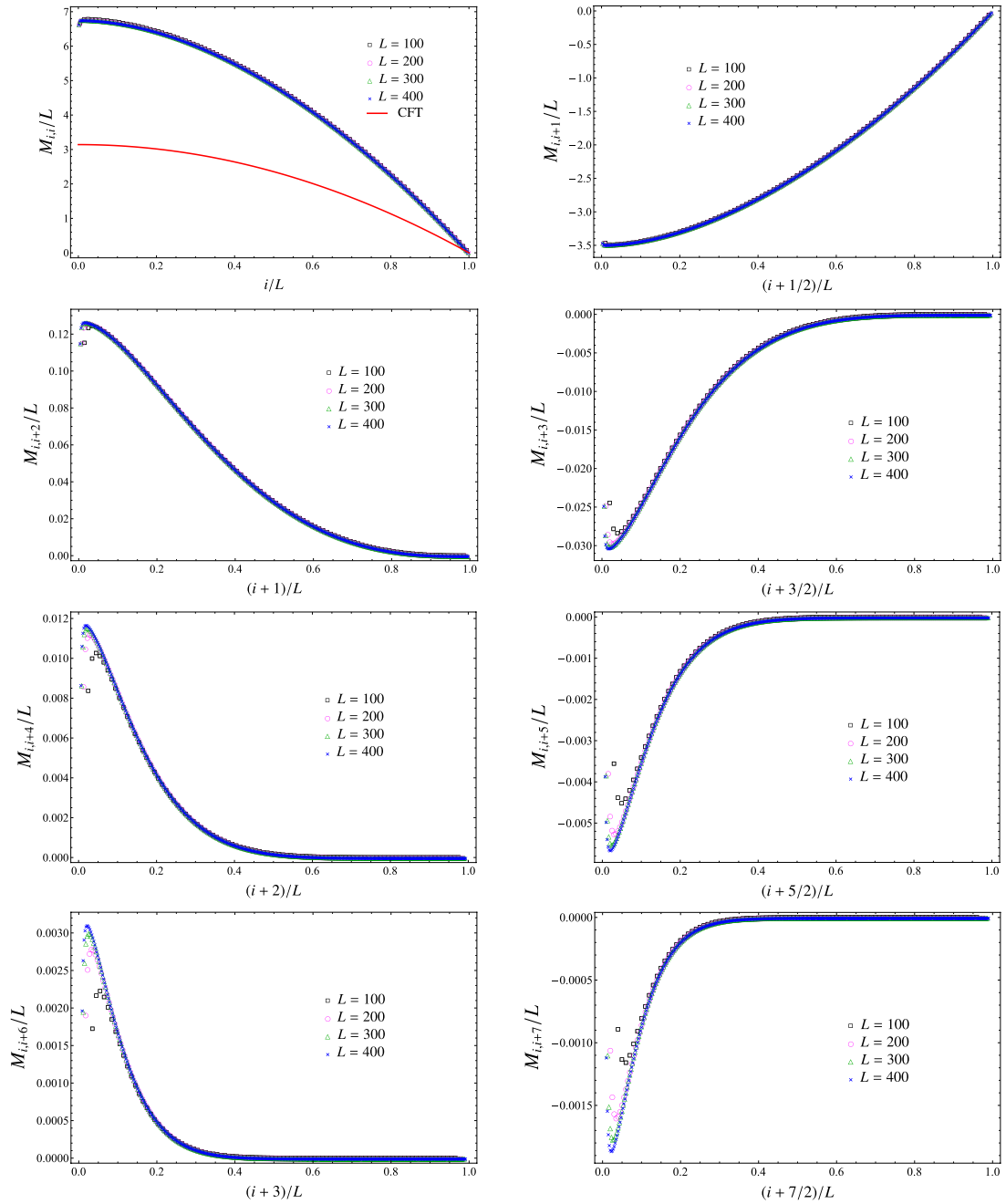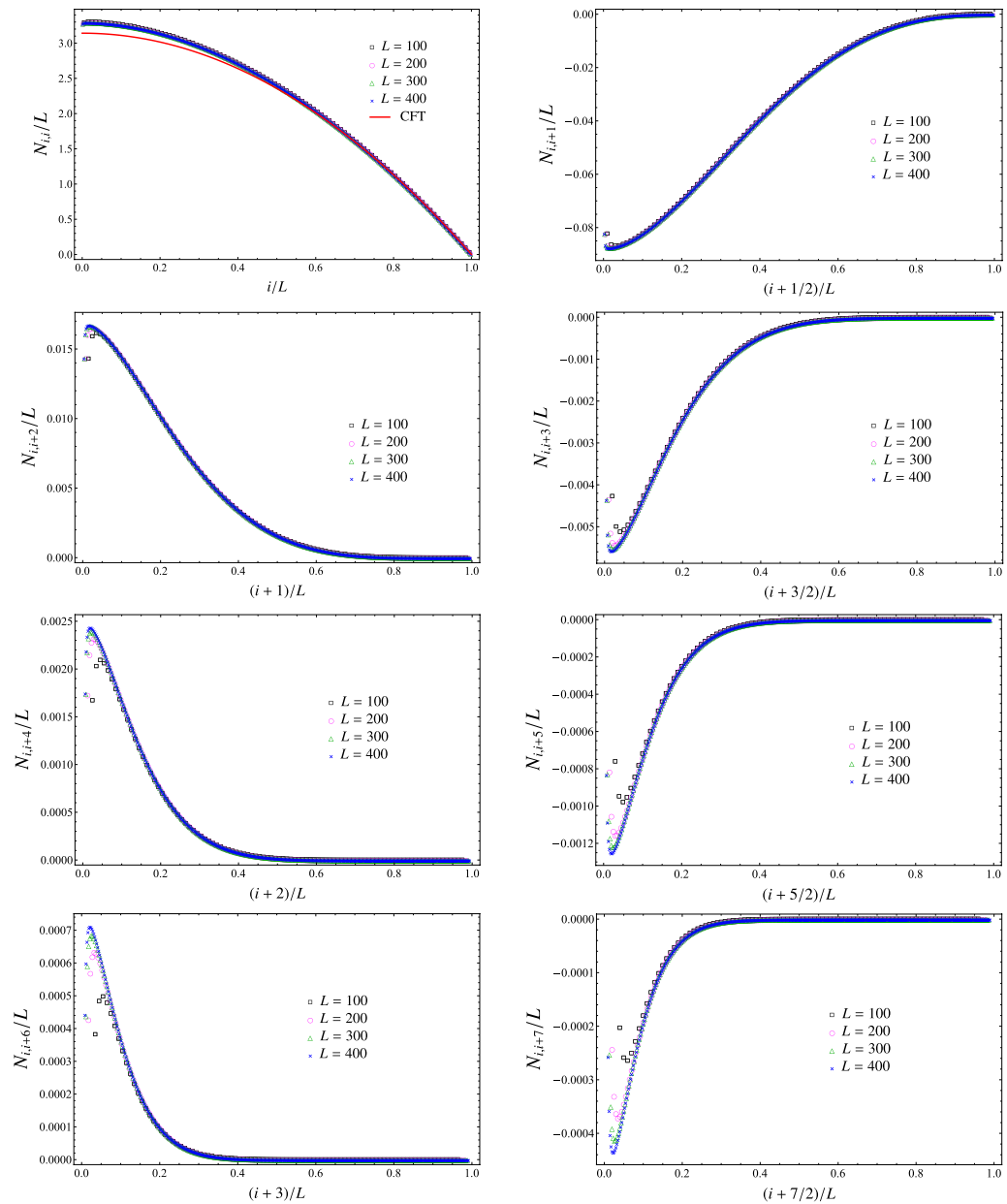
and

Figure 8. Diagonals of the matrix M (see (20)) when A is an interval with L sites at the beginning of the semi-infinite line and $\omega = 0$. The red solid curve is the half parabola (4).

$$\mathcal{M}_{1,k_{\max}}^{(2)}(x) \equiv \lim_{L \to \infty} \frac{\mathsf{M}_{1,k_{\max}}^{(2)}(i)}{L} \equiv \sum_{k=1}^{k_{\max}} k^2 \mu_{1,k}(x_k) \tag{68}$$

being

Figure 9. Diagonals of the matrix N (see (20)) when A is an interval with L sites at the beginning of the semi-infinite line and $\omega = 0$. The red solid curve is the half parabola (4).

$$\lim_{L \to \infty} \frac{M_{i+1,i+1+k} - M_{i,i+k}}{L} \equiv \mu_{1,k}(x_k) \tag{69}$$

where the subindex 1 means that these quantities are related to the first derivative of the functions $\mu_k(x)$. Taking $k_{\max} \to \infty$ in (68), we find

$$\mathcal{M}^{(2)}_{1,k_{\max}}(x) \longrightarrow \mathcal{M}^{(2)}_{1,\infty}(x). \tag{70}$$

Notice that we can also follow the steps performed in section 3.2 combining the last two terms within the square brackets in (66) into $\partial_x[\mu_k(x)\,\Phi(x)']$ and integrating by parts the corresponding integral, which provides the boundary terms $[\mu_k(x)\,\Phi'(x)\,\Phi(x)]|_{x=0}^{x=\ell}$. These terms do not contribute because $\mu_k(\ell) = 0$ at the entangling point and the Dirichlet boundary condition $\Phi(0) = 0$ holds at the beginning of the semi-infinite line.

Taking the limit $k_{\max} \to \infty$ in (66) and employing the weight functions introduced in (47), (48) and (70), for the non-vanishing contributions to the continuum limit of the entanglement Hamiltonian we find

$$\frac{H_M + H_N}{2} = \frac{\ell}{a^2} \int_0^\ell \frac{1}{2} \left[\mathcal{M}_\infty^{(0)}(x) + \frac{1}{4}\,\mathcal{M}_{2,\infty}^{(2)}(x) \right] \Phi(x)^2 \, \mathrm{d}x$$
$$+ \ell \int_0^\ell \frac{1}{2} \left[\mathcal{N}_\infty^{(0)}(x)\,\Pi(x)^2 + \mathcal{M}_{1,\infty}^{(2)}(x)\,\Phi'(x)\,\Phi(x) + \mathcal{M}_\infty^{(2)}(x)\,\Phi''(x)\,\Phi(x) \right] \mathrm{d}x. \quad (71)$$

We remark that, although some formal expressions also occur in the case of the interval in the infinite line in section 3.2, their values depend on the system that we are exploring through the correlators (64) and (65).

Also in the numerical analysis of this bipartition we have employed all the decompositions introduced in section 2 and in the appendix as a starting point. We find that the most effective approach is based on (50)–(53). For the interval at the beginning of the semi-infinite line, we also need the combination of the matrix elements of M for $\mathsf{M}_{1,k_{\max}}^{(2)}$ and it is not difficult to find that it reads

$$\mathsf{M}_{1,k_{\max}}^{(2)} = \begin{cases} \sum_{k=1}^{k_{\max}} k^2 \big(M_{i+1,i+1+k} - M_{i,i+k} \big) & 1 \leqslant i \leqslant L/2 \\ \sum_{k=1}^{k_{\max}} k^2 \big(M_{i-k+1,i+1} - M_{i-k,i} \big) & L/2 + 1 \leqslant i \leqslant L. \end{cases} \quad (72)$$

Like for the interval in the infinite line, the occurrence of two branches in (50)–(53) and (72) allows us to probe the entire interval. This cannot be done when the decompositions (14) and (15) are employed (see top panels of figures A4 and A5). Notice that, in contrast with section 3.2, in this case the reflection symmetry with respect to the centre of the interval is not expected.

In figure 10 we observe that the numerical data for $\mathsf{M}_{k_{\max}}^{(0)}(i)$, $\mathsf{M}_{1,k_{\max}}^{(2)}(i)$ and $L\,\mathsf{M}_{2,k_{\max}}^{(2)}(i)$ with $i \neq 1$ collapse on well-defined curves when L increases. As for some of the weight functions occurring in (71), these collapses support the following conjecture

$$\mathcal{M}_\infty^{(0)}(x) = 0 \qquad \mathcal{M}_{1,\infty}^{(2)}(x) = 0 \qquad \mathcal{M}_{2,\infty}^{(2)}(x) = 0 \quad (73)$$

for any fixed value of $x \in A$ such that $x \neq 0$. The insets on the right in all the panels of figure 10 highlight that the values of $\mathsf{M}_{k_{\max}}^{(0)}(i)/L$, $\mathsf{M}_{1,k_{\max}}^{(2)}(i)/L$ and $\mathsf{M}_{2,k_{\max}}^{(2)}(i)/L$ for $i = 1$ seem to converge to finite non-vanishing constants. Since $\mathcal{M}_\infty^{(0)}(0)$, $\mathcal{M}_{1,\infty}^{(2)}(0)$ and $\mathcal{M}_{2,\infty}^{(2)}(0)$ are multiplied by $\Phi(0)$ in (71), the Dirichlet boundary condition $\Phi(0) = 0$ implies that this feature does not provide a non-vanishing term in the continuum limit of the entanglement Hamiltonian. In the top panel of figure 10, the discontinuity in the centre of the interval is due to the fact that $\mathsf{M}_{k_{\max}}^{(0)}$ in (50) is defined through two branches. This discontinuity is not observed if different decompositions for the operators $\widehat{H}_M$ and $\widehat{H}_N$ in (13) are adopted.
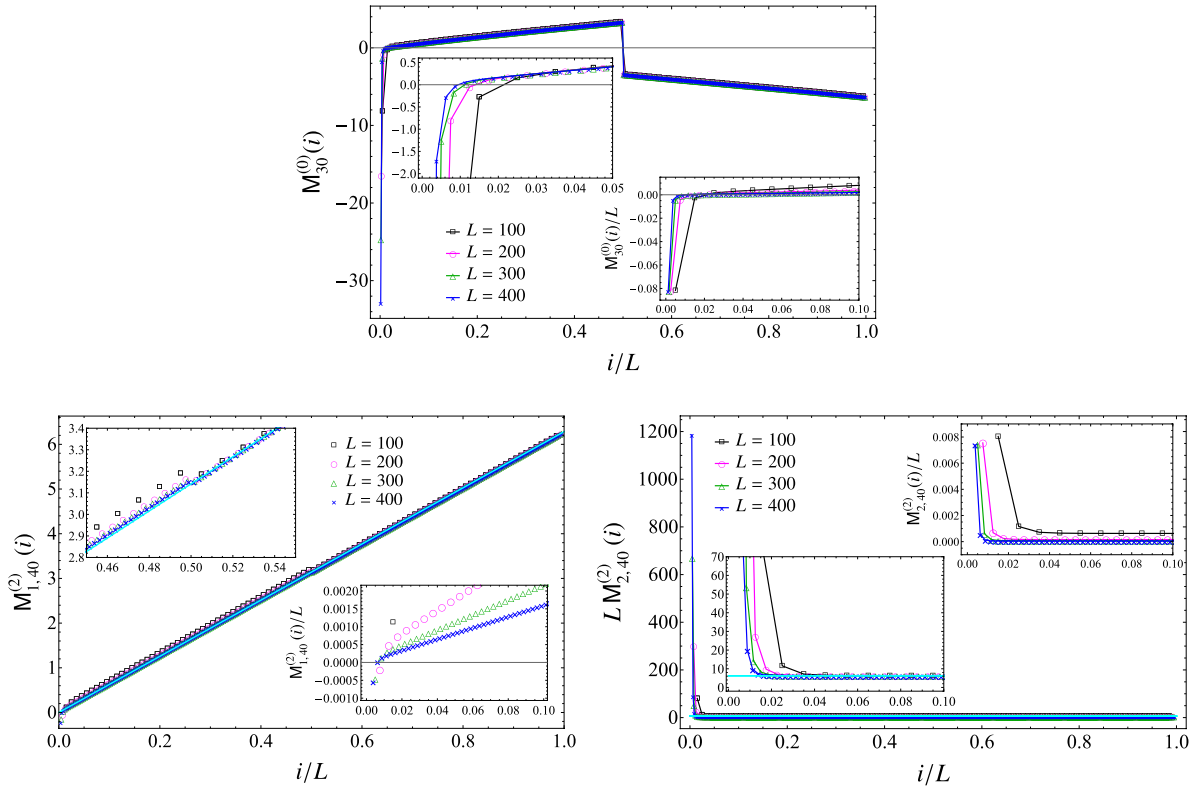
Figure 10. The combinations (50) (top), (72) (bottom left) and (53) (bottom right) when the subsystem is an interval made by L sites at the beginning of the semi-infinite line and $\omega = 0$. The cyan line in the bottom left panel corresponds to $2\pi(i/L)$, while the cyan horizontal line in the bottom right panel corresponds to 2π. The collapses of the data points for increasing values of L support (73).

In figure 11 we show $-\mathsf{M}_{k_{\max}}^{(2)}/L$ (left panel) and $\mathsf{N}_{k_{\max}}^{(0)}/L$ (right panel) for increasing values of L and an optimal value of $k_{\max}$ which guarantee certain stability of the numerical results. The collapses of the data points naturally lead to the conjecture that

$$\mathcal{M}_{\infty}^{(2)}(x) = -\beta(x) \qquad\qquad \mathcal{N}_{\infty}^{(0)}(x) = \beta(x) \tag{74}$$

where $\beta(x)$ is the half parabola (4) predicted by the CFT.

It is instructive to compare the results in figure 11 for the interval at the beginning of the semi-infinite line with the ones shown in figure 5 for the interval in the infinite line. From the insets of these figures we observe that in the former case larger values of L are needed to reach the CFT curve close to the origin of the semi-infinite line. This could be related to the fact that we are obtaining a CFT curve that is independent of the boundary conditions imposed at the origin of the semi-infinite line from numerical data that depend on them.

In the bottom panels of figure 10, the data points for $\mathsf{M}_{1,k_{\max}}^{(2)}$ and $L\,\mathsf{M}_{2,k_{\max}}^{(2)}(i)$ with $i \neq 1$ collapse on the cyan straight lines, which correspond respectively to $2\pi\,x/\ell = -\ell\beta'(x)$ and to $2\pi = -\ell^2\beta''(x)$ when L is large enough. Similarly to the case of the interval in the infinite line (see the final remarks of section 3.2), we can roughly justify this behaviour by noticing that $\mathsf{M}_{1,k_{\max}}^{(2)}$ and $\mathsf{M}_{2,k_{\max}}^{(2)}$ are obtained through finite differences
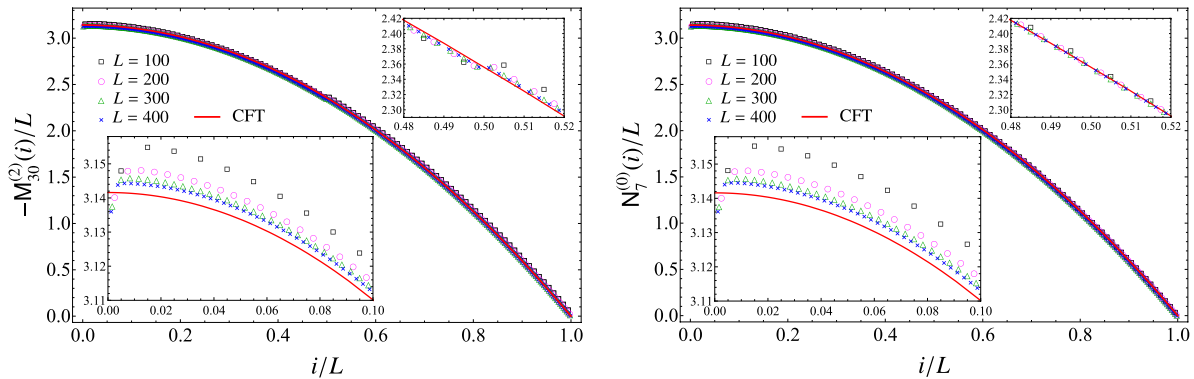
Figure 11. The combinations (52) (left) and (51) (right) when the subsystem is an interval made by L sites at the beginning of the semi-infinite line and $\omega = 0$. The collapses of the data points shown support (74), with $\beta(x)$ given by the half parabola (4) (red solid curve).

approximations of $\mu'_k(x)$ and $\mu''_k(x)$, respectively; hence, from (74), one expects to find respectively $-\beta(x)'$ and $-\beta(x)''$. Also, in this case, exchanging the derivatives with respect to x with the discrete sums over k leads to wrong results, as already discussed in the final part of section 3.2 for the interval in the infinite line.

In figure 12 we show again $-\mathsf{M}^{(2)}_{k_{\max}}/L$ and $\mathsf{N}^{(0)}_{k_{\max}}/L$, but for lower values of $k_{\max}$ in order to highlight the fact that the collapse of the numerical data onto the CFT curve improves as $k_{\max}$ increases. This behaviour is stabilised around optimal values for $k_{\max}$ that correspond to the data reported in figure 11. Furthermore, we encounter the same parity effect observed in figure 6 and mentioned in section 3.2, which is due also in this case to the fact that the kth diagonals of M and N have a definite sign related to the parity of k (see figures 8 and 9).

4.3. Entanglement spectrum

The BCFT analysis of the entanglement spectrum presented in [13], where (5) has been derived, includes the case that we are considering, given by the entire system in its ground state and the interval A at the beginning of the semi-infinite line. In this bipartition only one entangling point occurs; hence the UV cutoff ϵ is introduced by removing only a disk of radius ϵ around the entangling point. The resulting Euclidean spacetime has the topology of the annulus and in this case different conformal boundary conditions are allowed at the two boundaries. In our analysis we impose Dirichlet boundary conditions along the boundary corresponding to the beginning of the semi-infinite line.

The numerical analysis of the entanglement spectrum is performed as in section 3.3 and the crucial difference with respect to the interval in the infinite line is that the massless regime given by $\omega = 0$ is well defined. In this regime we observe that the lowest single-particle entanglement energy ε_1 is non-vanishing, in contrast with the case of the interval in the infinite line.

In the top left panel of figure 13 we show the numerical results for the single-particle entanglement energies ε_k/L in terms of k/L corresponding to some values of L, finding that they nicely collapse on a well-defined curve when L is large enough, like
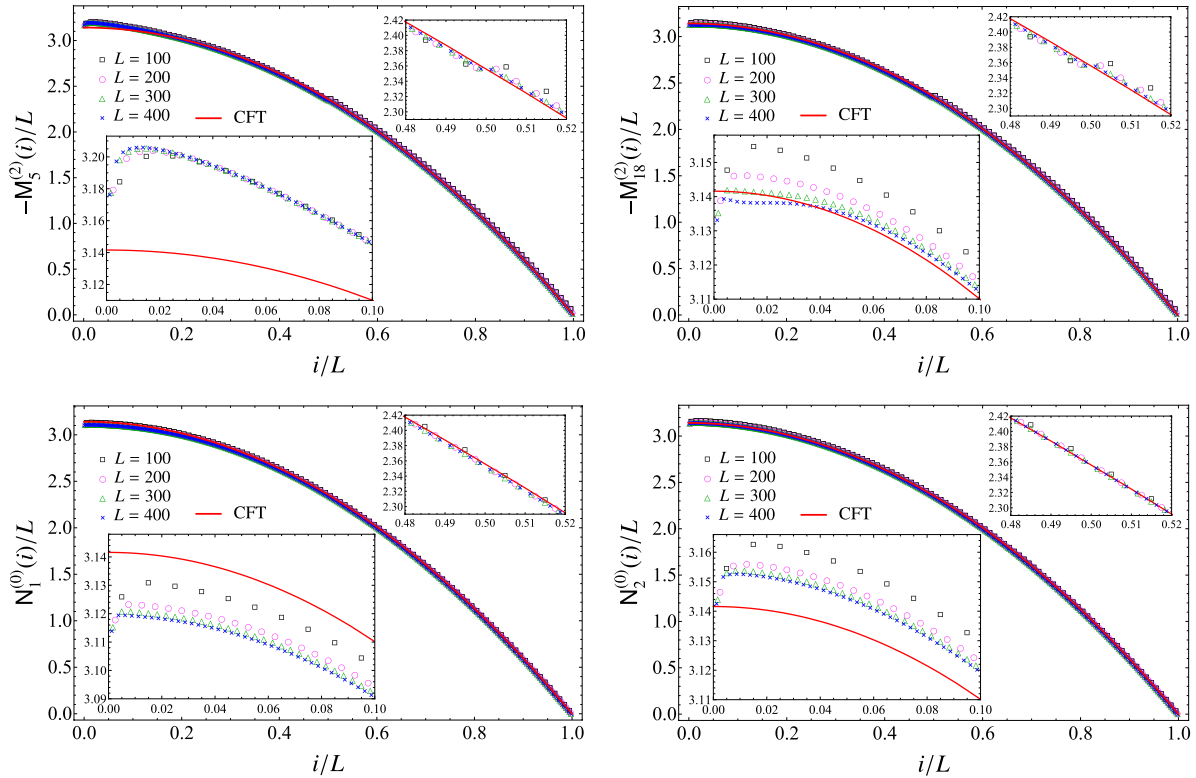
Figure 12. Role of the parameter k_{max} in the combinations (52) (top panels) and (51) (bottom panels) when the subsystem is an interval made by L sites at the beginning of the semi-infinite line and $\omega = 0$. The insets, which zoom in on the left endpoint and on the central part of the interval, show that the agreement with the CFT prediction given by the half parabola (4) (red solid curve) improves as k_{max} increases.

in the case of the interval in the infinite line (see the top right panel of figure 7). The curves obtained for these two spatial bipartitions are compared in the top right panel of figure 13, finding that they basically overlap, once the curve for the interval in the infinite line is multiplied by a factor of 2 (the insets highlight that this agreement is very good in the highest part of the spectrum and gets worse in the lowest part of the spectrum).

In the bottom panel of figure 13 we show the ratios g_r/g_1 between the generic gap g_r and the smallest gap g_1 in the entanglement spectrum as functions of $\log L$, for $1 \leqslant r \leqslant 13$. These ratios take all the integer values between 1 and 6 included (we checked that $g_r/g_1 > 6.5$ for $r > 13$ for the largest value of L at our disposal). This feature originates from the fact that in the low-lying part of the single-particle entanglement spectrum the eigenvalues are equally separated by an integer multiple of ε_1 (see also section 3.3). Comparing figures 13 and 7, it is straightforward to notice that g_r/g_1 take all the integer values for both the bipartitions, but the corresponding degeneracies are very different in the two cases. In particular, for the low-lying part of the single-particle entanglement spectrum the ratios $\varepsilon_r/\varepsilon_1$ take the integer odd numbers $1, 3, 5, 7 \ldots$ (see e.g. the top inset in the top right panel of figure 13). Plugging these values into the relation between ε_r and g_r, we find that g_r/g_1 take strictly positive integer values
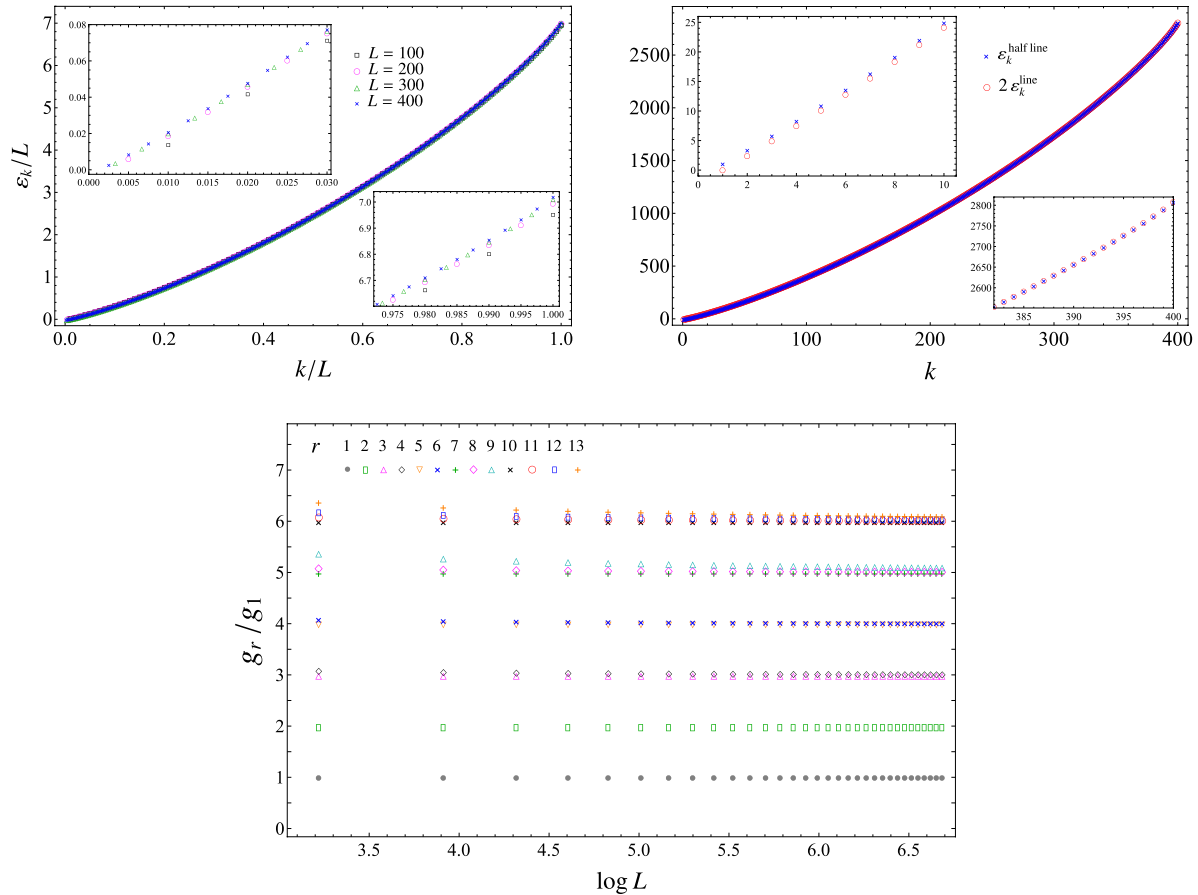
Figure 13. Entanglement spectrum for an interval at the beginning of the semi-infinite line with Dirichlet boundary conditions. Top left: the single-particle entanglement energies ε_k for different values of L (the insets zoom in on the lowest and highest values of k). Top right: comparison between the single-particle entanglement energies ε_k for an interval with $L = 400$ sites at the beginning of the semi-infinite line with Dirichlet boundary conditions (see the top left panel) and the ones for an interval with $L = 400$ sites in the infinite line (see the top right panel of figure 7). Bottom: the ratios of the gaps in the entanglement spectrum as functions of $\log L$ when $\omega = 0$.

n whose the degeneracy is given by the number of ways to write n as a sum of positive integers that are not repeated (see the bottom panel of figure 13).

The degeneracy observed in figure 13 is compatible with the conformal spectrum of the BCFT given by the free massless scalar on a segment with mixed boundary conditions, namely with Dirichlet boundary conditions imposed at one endpoint and Neumann boundary conditions at the other endpoint [33, 35]. As discussed e.g. in [33], in this case the Laurent expansion that we need is given by $\partial_z \Phi(z) = \sum_{n \in \mathbb{Z} + \frac{1}{2}} j_n \tilde{J}_n(z)$, where the functions $\tilde{J}_n$ form an orthonormal basis different from the one mentioned in section 3.3 and it is worth remarking that the index of the sum runs over half-integers. By constructing the Hilbert space as discussed in section 3.3, now we have that the conformal dimensions associated with the different states can take both integer or half-integer values. Thus, by writing strictly positive integer or half-integer numbers as sums of half-integers, one finds that g_r/g_1 take strictly positive integer values n whose

degeneracy is the number of ways to decompose n as a sum of non-repeated strictly positive integers.

Since in our analysis Dirichlet boundary conditions are imposed at the beginning of the semi-infinite line, we can conclude that Neumann boundary conditions must be imposed at the boundary introduced by the regularisation procedure around the entangling point. This allows us to fix the ambiguity found in section 3.3, concluding that the numerical results for the entanglement spectrum of the interval in the infinite line in the continuum limit agree with the conformal spectrum of the BCFT given by the free massless scalar on a segment with Neumann boundary conditions imposed on both the boundaries encircling the endpoints of the interval in the Euclidean spacetime. Also for this bipartition we expect that the agreement with the conformal spectrum of the BCFT holds only for the low-lying part of the entanglement spectrum.

5. Conclusions

In this manuscript we have performed a numerical analysis of the continuum limit of the entanglement Hamiltonians of a block made by L consecutive sites in massless harmonic chains, in the two cases where the subsystem is an interval in the infinite line or an interval at the beginning of the semi-infinite line with Dirichlet boundary conditions imposed at its endpoint. The procedure is based on the method introduced in [20, 22] for chains of free fermions, which has been adapted here to harmonic chains.

We have obtained the analytic expression (2) predicted by CFT, with the weight function $\beta(x)$ and the energy density $T_{00}(x)$ respectively given by (3) and (6) for the interval in the infinite line and by (4) and (7) for the interval at the beginning of a semi-infinite line. A remarkable agreement between the data points and the weight functions $\beta(x)$ predicted by CFT is observed (see figures 5 and 11). It would be instructive to support our numerical results with analytic computations, by first finding analytic expressions for the functions $\mu_k(x)$ and $\nu_k(x)$ (see figures 2 and 3 for the interval in the infinite line and figures 8 and 9 for the interval at the beginning of the semi-infinite line) and then by analytically calculating the sums involving these functions and their derivatives which provide the continuum limit of the entanglement Hamiltonians, as done in [20, 22] for the interval in the infinite chain of free fermions.

We have also explored the continuum limit of the entanglement spectra of these entanglement Hamiltonians, finding that the ratios of the low-lying gaps provide the ratios of the conformal dimensions of the BCFT given by the massless scalar on the annulus with the proper conformal boundary conditions, as predicted in [13] (see figures 7 and 13). The numerical results indicate that Neumann boundary conditions must be imposed along the boundaries introduced by the regularisation procedure. This is in agreement with a similar numerical analysis performed in lattice spin models [26], where it has been found that the numerical results for the entanglement spectra are compatible with the conformal spectra of BCFT with free boundary conditions imposed along the boundaries around the entangling points. This has also been confirmed by numerical studies out of equilibrium [28].

The results reported in this manuscript can be extended in various directions. In massless harmonic chains, the entanglement Hamiltonians of an interval in a circle when the system is in its ground state or in the infinite line when the system is at finite temperature should be studied because in these cases (2) still holds and the weight functions $\beta(x)$ are known from CFT [12, 13, 21, 22]. It is also natural to explore the entanglement Hamiltonians for bipartitions involving disjoint intervals [15, 16, 39], spatially inhomogeneous chains [14, 40] and higher dimensional quantum systems [11]. It is important to find explicit expressions for the entanglement Hamiltonians in interacting lattice models, both through analytic and numerical methods [41–45]. In addition, the analysis of the entanglement spectra [26, 34, 46–49] and of the contour for the entanglement entropies [30, 50, 51], which is a quantity strictly related to the entanglement Hamiltonian, deserve further analysis. It is also useful to study operators on the lattice that provide efficient approximations of the entanglement Hamiltonians [14, 52]. We also mention that, in order to understand the unitary time evolution of a system after a quantum quench, i.e. after a sudden change that drives the system out of equilibrium [53], relevant insights could come from the analysis of the time evolutions of the entanglement Hamiltonians and of their entanglement spectra [13, 27, 28, 54–56].

Acknowledgments

Appendix. Alternative summations and role of $k_{\max}$

In this appendix we report further results supporting the numerical analysis discussed in the main text. First we briefly discuss the choice of the numerical value of ωL adopted to study the entanglement Hamiltonian of the interval in the infinite line. In the remaining part of this appendix, we discuss some numerical results obtained through decompositions of the operators $\widehat{H}_M$ and $\widehat{H}_N$ in (13) that are different from (18) and (19).

The harmonic chain on the infinite line displays translation invariance and this symmetry leads to the occurrence of the zero mode, that prevents us from setting $\omega = 0$ in our numerical analysis, as already remarked in section 3.1. In order to study the entanglement Hamiltonians in the massless regime of this harmonic chain, we have to choose very small but non-vanishing values of $\omega > 0$. The high numerical precision required for our numerical analysis allows us to take $\omega > 0$ significantly close to zero. The numerical data reported in the figures discussed in sections 3.2 and 3.3 correspond to $\omega L = 10^{-500}$ and in figure A1 we justify this choice by showing $\mathsf{M}^{(2)}_{k_{\max}}/L$ and $\mathsf{N}^{(0)}_{k_{\max}}/L$ for decreasing values of ωL and for three increasing values of $k_{\max}$ at fixed $L = 400$. In
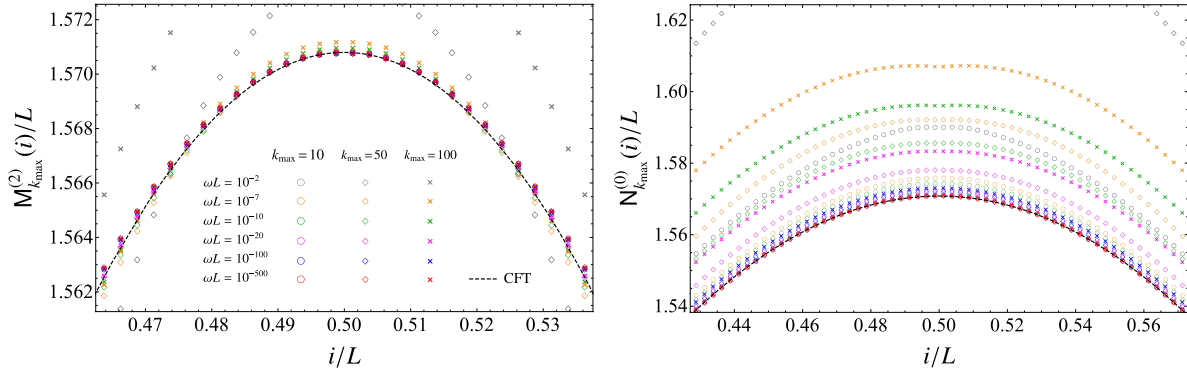
Figure A1. The combination (52) (left) and the combination (51) (right) for decreasing values of $\omega L \ll 1$ and increasing values of $k_{\max}$ when the subsystem is an interval made by $L = 400$ sites in the infinite chain. The dashed black line corresponds to the parabola (3) predicted by CFT.
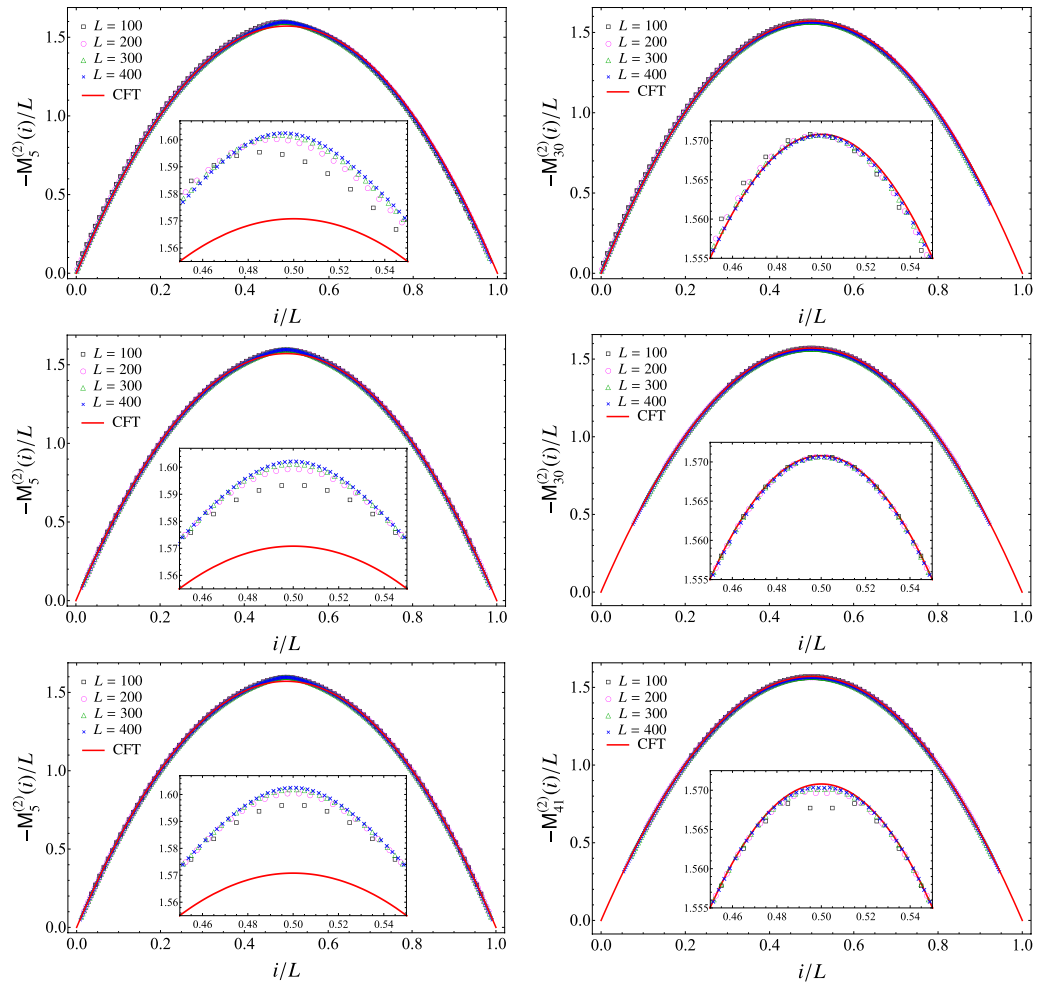

Figure A2. The combinations given by (42) (top panels), by the first expression in (A.1) (middle panels), and by (A.10) (bottom panels) for different values of L and two values of $k_{\max}$ for each combination (left and right panels), when the subsystem is an interval in the infinite line. The red solid curve is the parabola (3) predicted by CFT.
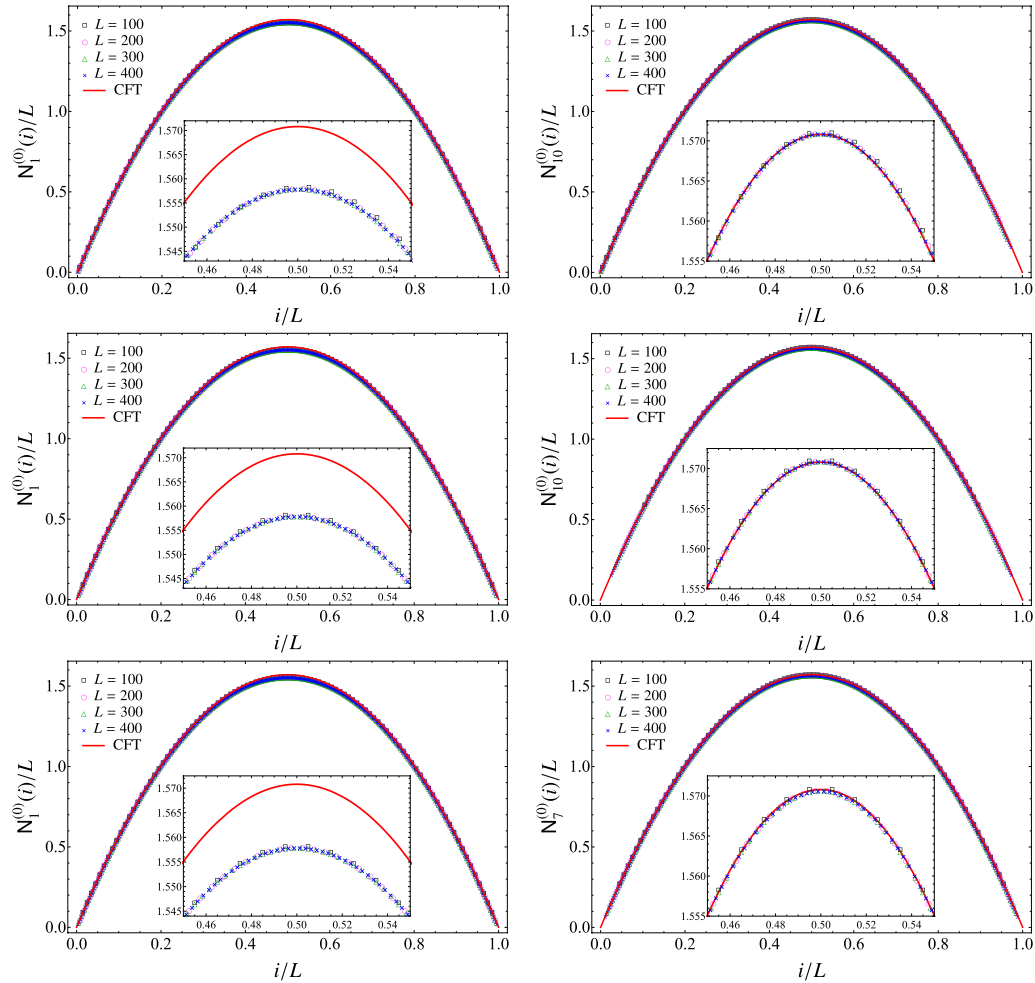
Figure A3. The combinations given by (39) (top panels), by the second expression in (A.1) (middle panels), and by (A.12) (bottom panels) for different values of L and two values of k_{max} for each combination (left and right panels), when the subsystem is an interval in the infinite line. The red solid curve is the parabola (3) predicted by CFT.

order to find a small value for $\omega L > 0$ that properly captures the features of the massless regime, we require that the numerical data are stabilised on the CFT prediction (3) for different values of k_{max}. While this condition is fulfilled already for $\omega L = 10^{-20}$ in the left panel of figure A1, it is not satisfied in the right panel. Instead, for $\omega L = 10^{-500}$ very good collapses on the CFT curve are observed for the data corresponding to different k_{max}.

In the main text we have discussed the results for the continuum limit reported in figures 4 and 5 for the interval in the infinite line (see section 3.2) and in figures 10 and 11 for the interval at the beginning of the semi-infinite line (see section 4.2). They have been obtained by starting from the decompositions (18) and (19) for $\widehat{H}_M$ and $\widehat{H}_N$, which lead to the combinations (50)–(53) for the interval in the infinite line, and to the same combinations together with (72) for the interval at the beginning of the semi-infinite line.
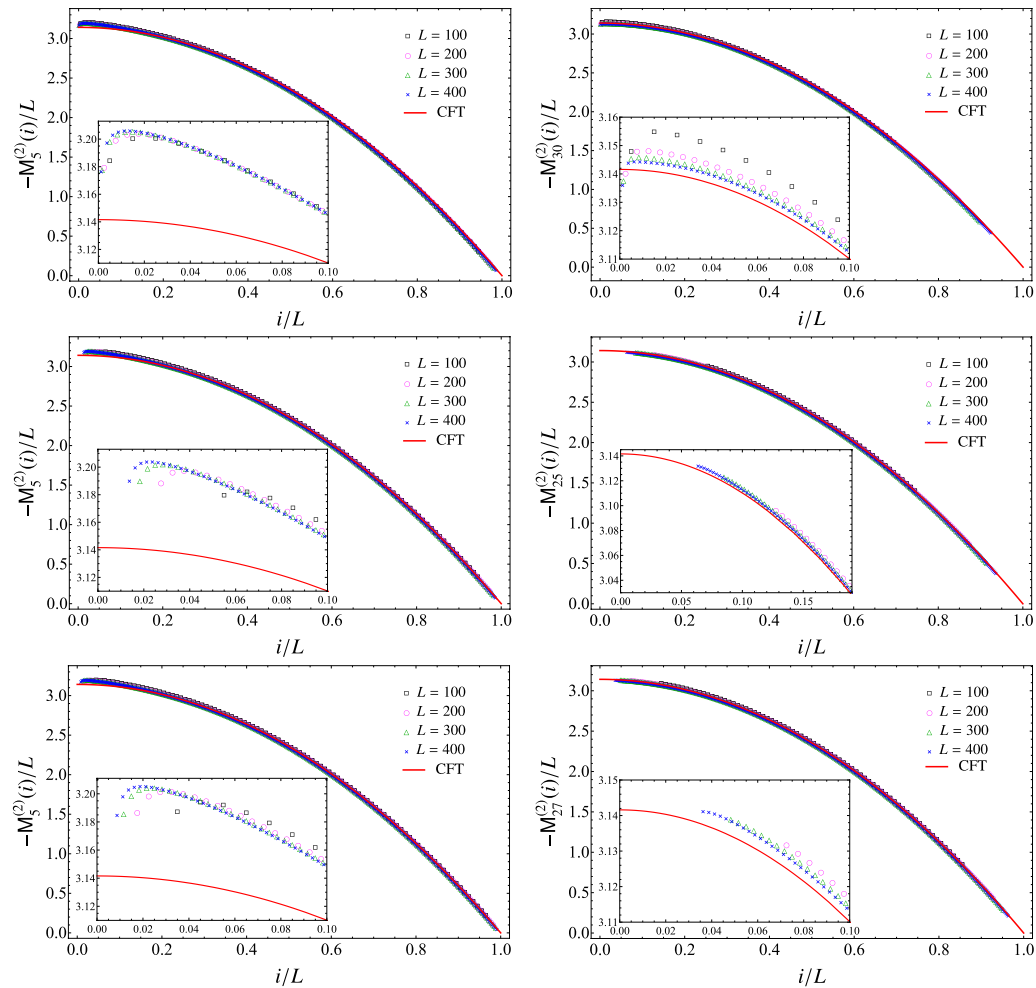
Figure A4. The combinations given by (42) (top panels), by the first expression in (A.1) (middle panels), and by (A.10) (bottom panels) for different values of L and two values of $k_{\max}$ for each combination (left and right panels), when the subsystem is an interval at the beginning of the semi-infinite line. The red solid curve is the half parabola (4) predicted by CFT.

The procedure to study the continuum limit starting from the decompositions (14) and (15) for $\widehat{H}_M$ and $\widehat{H}_N$, which provides the combinations (36), (39), (42) and (46) for the interval in the infinite line (see section 3.2) and the same combinations together with (67) for the interval at the beginning of the semi-infinite line (see section 4.2), has been explained in the main text. The numerical results of the combinations (42) and (39) for various sizes L of the intervals and for two values of $k_{\max}$ are shown in the top panels of figures A2 and A3 for the interval in the infinite line and of figures A4 and A5 for the interval at the beginning of the semi-infinite line. As $k_{\max}$ increases, the agreement between the data and the CFT predictions given by (3) and (4) improves. The numerical data stabilise around a value that has been adopted in the right panels. As for the combinations (36) and (46), we find that they lead to the function that vanishes identically in the interval, as expected from CFT. The range of the index i in these combinations does not allow us to capture the curve predicted by CFT on the entire
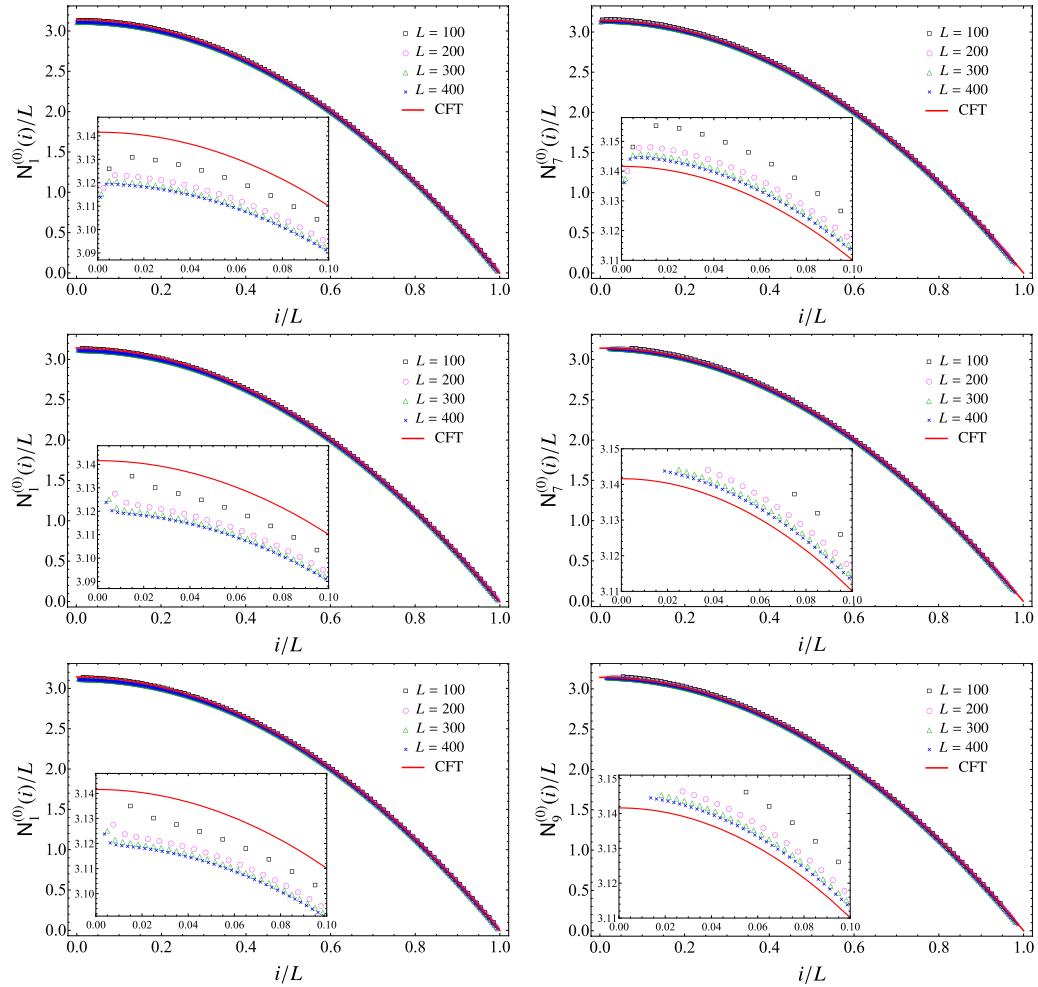
Figure A5. The combinations given by (39) (top panels), by the second expression in (A.1) (middle panels), and by (A.12) (bottom panels) for different values of L and two values of $k_{\max}$ for each combination (left and right panels), when the subsystem is an interval at the beginning of the semi-infinite line. The red solid curve is the half parabola (4) predicted by CFT.

interval and this fact motivated us to employ the decompositions (18) and (19) instead of (14) and (15).

In the remaining part of this appendix, we discuss the continuum limit of the entanglement Hamiltonians based on two other decompositions for $\widehat{H}_M$ and $\widehat{H}_N$ in (13).

Considering the decompositions (16) and (17), by adapting the procedure described in section 3.2, we find the combinations given by

$$\mathsf{M}_{k_{\max}}^{(2)}(i) = \sum_{k=-k_{\max}}^{k_{\max}} \frac{k^2}{2} M_{i,i+k} \qquad \mathsf{N}_{k_{\max}}^{(0)}(i) = \sum_{k=-k_{\max}}^{k_{\max}} N_{i,i+k} \tag{A.1}$$

and

$$\mathsf{M}_{k_{\max}}^{(0)}(i) = \sum_{k=-k_{\max}}^{k_{\max}} M_{i,i+k} \qquad \mathsf{M}_{2,k_{\max}}^{(2)}(i) = \sum_{k=-k_{\max}}^{k_{\max}} \frac{k^2}{2} \Big(M_{i+1,i+1+k} - 2M_{i,i+k} + M_{i-1,i-1+k} \Big) \tag{A.2}$$

where $1 + k_{\max} \leqslant i \leqslant L - k_{\max}$. We emphasise that the combinations (A.1) have also been found in [19] by employing a different approach. The data obtained through the combinations (A.1) are shown in the middle panels of figures A2 and A3 for the interval in the infinite line and of figures A4 and A5 for the interval at the beginning of the semi-infinite line. Also in this case the agreement with the CFT predictions (3) and (4) improves as $k_{\max}$ increases until it reaches an optimal value corresponding to the one adopted in the right panels. Comparing the middle panels with the top panels and with figures 5, 6, 11 and 12, it is straightforward to notice that (A.1) does not allow us to describe the CFT curves close to both the endpoints of the interval. The data corresponding to (A.2), that are not reported in this manuscript, provide the function that vanishes identically in the interval as L increases and for optimal values of $k_{\max}$, as expected from the CFT analysis.

Another way to obtain the results predicted by CFT in the continuum limit can be introduced by adapting the method employed in the numerical analysis of [22] for the entanglement Hamiltonian of an interval in an infinite chain of free fermions. Considering only blocks containing an even number L of sites, let us decompose the operators $\widehat{H}_M$ and $\widehat{H}_N$ in (13) respectively as

$$
\widehat{H}_M = L \sum_{i=1}^{L} \frac{M_{i,i}}{L} \, \hat{q}_i^2
$$
$$
+ 2L \left(\sum_{k=1}^{L/2-1} \sum_{i=1+k}^{L-k} \frac{M_{i-k,i+k}}{L} \, \hat{q}_{i-k} \, \hat{q}_{i+k} + \sum_{k=0}^{L/2-1} \sum_{i=1+k}^{L-k-1} \frac{M_{i-k,i+k+1}}{L} \, \hat{q}_{i-k} \, \hat{q}_{i+k+1} \right) \quad \text{(A.3)}
$$

and

$$
\widehat{H}_N = L \sum_{i=1}^{L} \frac{N_{i,i}}{L} \, \hat{p}_i^2
$$
$$
+ 2L \left(\sum_{k=1}^{L/2-1} \sum_{i=1+k}^{L-k} \frac{N_{i-k,i+k}}{L} \, \hat{p}_{i-k} \, \hat{p}_{i+k} + \sum_{k=0}^{L/2-1} \sum_{i=1+k}^{L-k-1} \frac{N_{i-k,i+k+1}}{L} \, \hat{p}_{i-k} \, \hat{p}_{i+k+1} \right) \quad \text{(A.4)}
$$

where we have separated the contributions of the even diagonals of M and N from the contributions of the odd diagonals.

In (A.3) and (A.4) the index i labels the elements along the diagonals of M and N, while in the decompositions introduced in section 2 it corresponds to a row index. Treating separately the contributions of the odd diagonals and of the even diagonals in (A.3) and (A.4) and using (29), (30) and (31), we can adapt the procedure described in section 3.2 to these decompositions of the operators $\widehat{H}_M$ and $\widehat{H}_N$. In this case we find that the combinations of diagonals occurring at the leading order as $a \to 0$ are

$$
\mathsf{M}_{r_{\max}}^{\mathrm{e}\,(0)}(i) \equiv M_{i,i} + 2 \sum_{r=1}^{r_{\max}} M_{i-r,i+r} \qquad \mathsf{M}_{r_{\max}}^{\mathrm{o}\,(0)}(i) \equiv M_{i,i} + 2 \sum_{r=1}^{r_{\max}} M_{i-r,i+r+1} \quad \text{(A.5)}
$$

which come from the even and odd diagonals, respectively.

The next subleading order in the expansion of the entanglement Hamiltonian as $a \to 0$ gets contributions both from $\widehat{H}_M$ and $\widehat{H}_N$. In particular, the continuum limit of $\widehat{H}_M$ to this order gives

$$\mathsf{M}^{\mathrm{e}\,(2)}_{r_{\max}}(i) \equiv \sum_{r=1}^{r_{\max}} (2r)^2\, M_{i-r,i+r} \qquad\qquad \mathsf{M}^{\mathrm{o}\,(2)}_{r_{\max}}(i) \equiv \sum_{r=1}^{r_{\max}} (2r+1)^2\, M_{i-r,i+r+1} \quad \text{(A.6)}$$

and the term originating from the finite difference approximation of $\mu_k''(x)$, namely

$$\mathsf{M}^{\mathrm{e}\,(2)}_{2,r_{\max}}(i) \equiv \sum_{r=1}^{r_{\max}} (2r)^2 \left(M_{i-r+1,i+r+1} - 2M_{i-r,i+r} + M_{i-r-1,i+r-1} \right)$$

$$\text{(A.7)}$$

$$\mathsf{M}^{\mathrm{o}\,(2)}_{2,r_{\max}}(i) \equiv \sum_{r=1}^{r_{\max}} (2r+1)^2 \left(M_{i-r+1,i+r+2} - 2M_{i-r,i+r+1} + M_{i-r-1,i+r} \right)$$

while from $\widehat{H}_N$ we find only

$$\mathsf{N}^{\mathrm{e}\,(0)}_{r_{\max}}(i) \equiv N_{i,i} + 2\sum_{r=1}^{r_{\max}} N_{i-r,i+r} \qquad\qquad \mathsf{N}^{\mathrm{o}\,(0)}_{r_{\max}}(i) \equiv N_{i,i} + 2\sum_{r=1}^{r_{\max}} N_{i-r,i+r+1}. \quad \text{(A.8)}$$

Notice that the range of the index i in the above expression is $1 + r_{\max} \leqslant i \leqslant L - (1 + r_{\max})$ for the combinations coming from the odd diagonals and $r_{\max} + 1 \leqslant i \leqslant L - r_{\max}$ for the combinations coming from the even diagonals.

The final expressions providing the continuum limit of the entanglement Hamiltonian are proper combinations of the terms coming from the even and odd diagonals, but in constructing these combinations we encounter the problem that the former ones are defined on $L - 2r_{\max}$ sites, while in the latter ones the index i assumes $L - 2r_{\max} - 1$ values. In this case the index i labels the elements along the diagonals; hence, focussing e.g. on (A.6), we encounter an ambiguity in the way to combine $\mathsf{M}^{\mathrm{o}\,(2)}_{r_{\max}}(i)$ with $\mathsf{M}^{\mathrm{e}\,(2)}_{r_{\max}}(i)$. In the following, first we split $\mathsf{M}^{\mathrm{o}\,(2)}_{r_{\max}}(i)$ as $\alpha\,\mathsf{M}^{\mathrm{o}\,(2)}_{r_{\max}}(i) + \beta\,\mathsf{M}^{\mathrm{o}\,(2)}_{r_{\max}}(i)$, with $\alpha + \beta = 1$. Then, in the sum between the even and the odd part, we choose to associate $\alpha\,\mathsf{M}^{\mathrm{o}\,(2)}_{r_{\max}}(i)$ to $\mathsf{M}^{\mathrm{e}\,(2)}_{r_{\max}}(i)$ and $\beta\,\mathsf{M}^{\mathrm{o}\,(2)}_{r_{\max}}(i)$ to $\mathsf{M}^{\mathrm{e}\,(2)}_{r_{\max}}(i+1)$. The values of α and β are not fixed uniquely and we choose $\alpha = \beta = 1/2$ in our numerical analysis. For the interval in the infinite line, this choice guarantees the expected symmetry with respect to the centre of the interval at finite L.

By applying this procedure to all the expressions in (A.5)–(A.8), we obtain respectively

$$\mathsf{M}^{(0)}_{k_{\max}}(i) = \mathsf{M}^{\mathrm{e}\,(0)}_{r_{\max}}(i) + \frac{1}{2}\left(\mathsf{M}^{\mathrm{o}\,(0)}_{r_{\max}}(i-1) + \mathsf{M}^{\mathrm{o}\,(0)}_{r_{\max}}(i) \right) \qquad\qquad \text{(A.9)}$$

$$\mathsf{M}^{(2)}_{k_{\max}}(i) = \mathsf{M}^{\mathrm{e}\,(2)}_{r_{\max}}(i) + \frac{1}{2}\left(\mathsf{M}^{\mathrm{o}\,(2)}_{r_{\max}}(i-1) + \mathsf{M}^{\mathrm{o}\,(2)}_{r_{\max}}(i) \right) \qquad\qquad \text{(A.10)}$$

$$\mathsf{M}^{(2)}_{2,k_{\max}}(i) = \mathsf{M}^{\mathrm{e}\,(2)}_{2,r_{\max}}(i) + \frac{1}{2}\left(\mathsf{M}^{\mathrm{o}\,(2)}_{2,r_{\max}}(i-1) + \mathsf{M}^{\mathrm{o}\,(2)}_{2,r_{\max}}(i) \right) \qquad\qquad \text{(A.11)}$$

$$\mathsf{N}^{(0)}_{k_{\max}}(i) = \mathsf{N}^{\mathrm{e}\,(0)}_{r_{\max}}(i) + \frac{1}{2}\left(\mathsf{N}^{\mathrm{o}\,(0)}_{r_{\max}}(i-1) + \mathsf{N}^{\mathrm{o}\,(0)}_{r_{\max}}(i) \right) \qquad\qquad \text{(A.12)}$$

where $r_{\max} + 1 \leqslant i \leqslant L - (r_{\max} + 1)$ and we have employed the parameter $k_{\max} = 2r_{\max} + 1$ adopted throughout this manuscript to label the last diagonal occurring in a particular combination of diagonals. Since we always choose odd $k_{\max}$ in our numerical analysis, the same number of even and odd diagonals occurs in the above combinations.

The numerical results for (A.10) and (A.12) are reported respectively in the left and right bottom panels of figures A2 and A3 for the interval in the infinite line and of figures A4 and A5 for the interval at the beginning of the semi-infinite line. As L and $k_{\max}$ increase, with $k_{\max} \ll L$, we observe again that the agreement of the numerical data with the CFT curves (3) and (4) improves. Nonetheless, since $r_{\max} + 1 \leqslant i \leqslant L - (r_{\max} + 1)$, the data points cannot capture the CFT curves close to the endpoints of the interval. We have also checked that, by performing this numerical analysis for (A.9) and (A.11), the vanishing curve is obtained everywhere within the interval except in the left endpoint in the case of the semi-infinite line, where the Dirichlet boundary conditions are imposed. These results also confirm the CFT predictions.

References

[1] Peschel I and Eisler V 2009 *J. Phys. A: Math. Theor.* **42** 504003
[2] Casini H and Huerta M 2009 *J. Phys. A: Math. Theor.* **42** 504007
[3] Amico L, Fazio R, Osterloh A and Vedral V 2008 *Rev. Mod. Phys.* **80** 517
   Calabrese P and Cardy J 2009 *J. Phys. A: Math. Theor.* **42** 504005
   Eisert J, Cramer M and Plenio M B 2010 *Rev. Mod. Phys.* **82** 277
[4] Nishioka T, Ryu S and Takayanagi T 2009 *J. Phys. A: Math. Theor.* **42** 504008
   Rangamani M and Takayanagi T 2017 Holographic Entanglement Entropy (Berlin, Springer)
[5] Islam R, Ma R, Preiss P, Tai M, Lukin A, Rispoli M and Greiner M 2015 *Nature* **528** 77
   Kaufman A, Tai M, Lukin A, Rispoli M, Schittko R, Preiss P and Greiner M 2016 *Science* **353** 794
[6] Bombelli L, Koul R, Lee J and Sorkin R 1986 *Phys. Rev.* D **34** 373
   Srednicki M 1993 *Phys. Rev. Lett.* **71** 666
   Callan C and Wilczek F 1994 *Phys. Lett.* B **333**
[7] Holzhey C, Larsen F and Wilczek F 1994 *Nucl. Phys.* B **424** 443
[8] Calabrese P and Cardy J 2004 *J. Stat. Mech.* P06002
[9] Bisognano J and Wichmann E 1975 *J. Math. Phys.* **16** 985
   Bisognano J and Wichmann E 1976 *J. Math. Phys.* **17** 303
[10] Hislop P and Longo R 1982 *Commun. Math. Phys.* **84** 71
[11] Casini H, Huerta M and Myers R 2011 *J. High Energy Phys.* JHEP05(2011)036
[12] Wong G, Klich I, Pando Zayas L and Vaman D 2013 *J. High Energy Phys.* JHEP12(2013)020
[13] Cardy J and Tonni E 2016 *J. Stat. Mech.* 123103
[14] Tonni E, Rodríguez-Laguna J and Sierra G 2018 *J. Stat. Mech.* 043105
[15] Casini H and Huerta M 2009 *Class. Quantum Grav.* **26** 185005
   Longo R, Martinetti P and Rehren K-H 2010 *Rev. Math. Phys.* **22** 331
[16] Arias R, Casini H, Huerta M and Pontello D 2018 *Phys. Rev.* D **98** 125008
[17] Peschel I and Chung M 1999 *J. Phys. A: Math. Gen.* **48** 8419
   Chung M and Peschel I 2000 *Phys. Rev.* B **62** 4191
   Chung M and Peschel I 2001 *Phys. Rev.* B **64** 064412
   Peschel I 2003 *J. Phys. A: Math. Gen.* **36** L205
   Cheong S and Henley C 2004 *Phys. Rev.* B **69** 075112
   Eisler V, Karevski D, Platini T and Peschel I 2008 *J. Stat. Mech.* P01023
   Eisler V and Peschel I 2013 *J. Stat. Mech.* P04028
   Arias R, Casini H, Huerta M and Pontello D 2017 *Phys. Rev.* D **96** 105019
[18] Peschel I 2004 *J. Stat. Mech.* P06004
[19] Arias R, Blanco D, Casini H and Huerta M 2017 *Phys. Rev.* D **95** 065005
[20] Eisler V and Peschel I 2017 *J. Phys. A: Math. Theor.* **50** 284003
[21] Eisler V and Peschel I 2018 *J. Stat. Mech.* 104001
[22] Eisler V, Tonni E and Peschel I 2019 *J. Stat. Mech.* 073101

[23] Li H and Haldane F D M 2008 *Phys. Rev. Lett.* **101** 010504
[24] Ohmori K and Tachikawa Y 2015 *J. Stat. Mech.* P04010
[25] Cardy J 1986 *Nucl. Phys.* B **275** 200
     Cardy J 1989 *Nucl. Phys.* B **324** 581
     Saleur H and Bauer M 1989 *Nucl. Phys.* B **320** 591
     Cardy J 1988 *Conformal Invariance and Statistical Mechanics* (*Lectures Delivered at Les Houches*) ed
        J Cardy (arXiv:hep-th/0411189)
[26] Läuchli A 2013 (arXiv:1303.0741)
[27] Di Giulio G, Arias R and Tonni E 2019 *J. Stat. Mech.* 123103
[28] Surace J, Tagliacozzo L and Tonni E 2019 (arXiv:1909.07381)
[29] Liguori A and Mintchev M 1998 *Nucl. Phys.* B **522** 345
[30] Botero A and Reznik B 2004 *Phys. Rev.* A **70** 052329
[31] Altland A and Simons B 2010 *Condensed Matter Field Theory* (Cambridge: Cambridge University Press)
[32] Callan C and Klebanov I 1994 *Phys. Rev. Lett.* **72** 1968
     Callan C, Klebanov I, Ludwig A and Maldacena J 1994 *Nucl. Phys.* B **422** 417
[33] Blumenhagen R and Plauschinn E 2009 *Introduction to Conformal Field Theory* (Berlin: Springer)
[34] Herwerth B, Sierra G, Cirac J and Nielsen A 2018 *Phys. Rev.* B **98** 115156
[35] Mussardo G 2009 *Statistical Field Theory: An Introduction to Exactly Solved Models in Statistical
        Physics* (Oxford: Oxford University Press)
[36] Lievens S, Stoilova N and Van der Jeugt J 2008 *J. Math. Phys.* **49** 073502
[37] Calabrese P, Cardy J and Tonni E 2013 *J. Stat. Mech.* P02008
[38] Taddia L, Xavier J, Alcaraz F and Sierra G 2013 *Phys. Rev.* B **88** 075112
[39] Furukawa S, Pasquier V and Shiraishi J 2009 *Phys. Rev. Lett.* **102** 170602
     Caraglio M and Gliozzi F 2008 *J. High Energy Phys.* JHEP11(2008)076
     Calabrese P, Cardy J and Tonni E 2009 *J. Stat. Mech.* P11001
     Fagotti M and Calabrese P 2010 *J. Stat. Mech.* P04016
     Calabrese P, Cardy J and Tonni E 2011 *J. Stat. Mech.* P01021
     Alba V, Tagliacozzo L and Calabrese P 2011 *J. Stat. Mech.* P06012
     Cardy J 2013 *J. Phys. A: Math. Theor.* **46** 285402
     Coser A, Tagliacozzo L and Tonni E 2014 *J. Stat. Mech.* P01008
     De Nobili C, Coser A and Tonni E 2015 *J. Stat. Mech.* P06021
     Coser A, Tonni E and Calabrese P 2016 *J. Stat. Mech.* 053109
[40] Allegra N, Dubail J, Stéphan J and Viti J 2016 *J. Stat. Mech.* 053108
     Dubail J, Stéphan J, Viti J and Calabrese P 2017 *SciPost Phys.* **2** 002
[41] Nienhuis B, Campostrini M and Calabrese P 2009 *J. Stat. Mech.* P02063
[42] Peschel I and Truong T 1987 *Z. Phys.* B **69** 385–91
     Itoyama H and Thacker H 1987 *Phys. Rev. Lett.* **58** 1395
     Peschel I, Kaulke M and Legeza O 1999 *Ann. Phys., NY* **8** 153
[43] Parisen Toldin F and Assaad F 2018 *Phys. Rev. Lett.* **121** 200602
[44] Cho G, Ludwig A and Ryu S 2017 *Phys. Rev.* B **95** 115122
[45] Klich I, Vaman D and Wong G 2017 *Phys. Rev. Lett.* **119** 120401
     Klich I, Vaman D and Wong G 2018 *Phys. Rev.* B **98** 035134
     Wong G 2019 *J. High Energy Phys.* JHEP2019(2019)45
     Blanco D and Perez-Nadal G 2019 *Phys. Rev.* D **100** 025003
     Blanco D, Garbarz A and Perez-Nadal G 2019 *J. High Energy Phys.* JHEP2019(2019)76
     Fries P and Reyes I 2019 *Phys. Rev. Lett.* **123** 211603
[46] Calabrese P and Lefevre A 2008 *Phys. Rev.* A **78** 032329
[47] Alba V, Haque M and Läuchli A 2012 *Phys. Rev. Lett.* **108** 227201
[48] Assaad F, Lang T and Parisen Toldin F 2014 *Phys. Rev.* B **89** 125121
     Assaad F 2015 *Phys. Rev.* B **91** 125146
[49] Alba V, Calabrese P and Tonni E 2018 *J. Phys. A: Math. Theor.* **51** 024001
[50] Chen Y and Vidal G 2014 *J. Stat. Mech.* P10011
[51] Coser A, De Nobili C and Tonni E 2017 *J. Phys. A: Math. Theor.* **50** 314001
[52] Dalmonte M, Vermersch B and Zoller P 2018 *Nat. Phys.* **14** 827–31
     Giudici G, Mendes-Santos T, Calabrese P and Dalmonte M 2018 *Phys. Rev.* B **98** 134403

Mendes-Santos T, Giudici G, Dalmonte M and Rajabpour M 2019 *Phys. Rev.* B **100** 155122

[53] Calabrese P and Cardy J 2005 *J. Stat. Mech.* P04010
Calabrese P and Cardy J 2006 *Phys. Rev. Lett.* **96** 136801
Calabrese P and Cardy J 2007 *J. Stat. Mech.* P06008

[54] Torlai G, Tagliacozzo L and De Chiara G 2014 *J. Stat. Mech.* P06001

[55] Wen X, Ryu S and Ludwig A 2018 *J. Stat. Mech.* 113103

[56] Zhu W, Huang Z, He Y and Wen X 2019 (arXiv:1909.08808)